The Astronomical Journal, 147:128 (18pp), 2014 June doi:10.1088/0004-6256/147/6/128

HAT-P-44b, HAT-P-45b, AND HAT-P-46b: THREE TRANSITING HOT JUPITERS IN POSSIBLE MULTI-PLANET SYSTEMS*

J. D. Hartman[1], G. Á. Bakos[1,16,17], G. Torres[2], G. Kovács[3,4], J. A. Johnson[5], A. W. Howard[6], G. W. Marcy[7], D. W. Latham[2], A. Bieryla[2], L. A. Buchhave[8], W. Bhatti[1], B. Béky[2], Z. Csubry[1], K. Penev[1], M. de Val-Borro[1], R. W. Noyes[2], D. A. Fischer[9], G. A. Esquerdo[2], M. Everett[10], T. Szklenár[11], G. Zhou[12], D. Bayliss[12], A. Shporer[5,13,14], B. J. Fulton[6], R. Sanchis-Ojeda[15], E. Falco[2], J. Lázár[11], I. Papp[11], and P. Sári[11]
[1] Department of Astrophysical Sciences, Princeton University, Princeton, NJ 08544, USA; jhartman@astro.princeton.edu
[2] Harvard-Smithsonian Center for Astrophysics, Cambridge, MA 02138, USA
[3] Konkoly Observatory, Budapest, Hungary
[4] Department of Physics and Astrophysics, University of North Dakota, Grand Forks, ND 58202-7129, USA
[5] Department of Astrophysics, California Institute of Technology, Pasadena, CA 91125, USA
[6] Institute for Astronomy, University of Hawaii, Honolulu, HI 96822, USA
[7] Department of Astronomy, University of California, Berkeley, CA 94720, USA
[8] Niels Bohr Institute, Copenhagen University, DK-2100 Copenhagen, Denmark
[9] Department of Astronomy, Yale University, New Haven, CT 06520-8101, USA
[10] National Optical Astronomy Observatory, 950 North Cherry Avenue, Tucson, AZ 85719, USA
[11] Hungarian Astronomical Association, 1461 Budapest, Hungary
[12] Research School of Astronomy and Astrophysics, Australian National University, Canberra, ACT 2611, Australia
[13] Las Cumbres Observatory Global Telescope Network, 6740 Cortona Drive, Suite 102, Santa Barbara, CA 93117, USA
[14] Department of Physics, Broida Hall, University of California, Santa Barbara, CA 93106, USA
[15] Kavli Institute for Astrophysics and Space Research, Massachusetts Institute of Technology, Cambridge, MA 02139, USA
Received 2013 August 13; accepted 2014 March 10; published 2014 April 24

ABSTRACT

We report the discovery by the HATNet survey of three new transiting extrasolar planets orbiting moderately bright ($V = 13.2$, 12.8, and 11.9) stars. The planets have orbital periods of 4.3012, 3.1290, and 4.4631 days, masses of 0.35, 0.89, and 0.49 M_J, and radii of 1.24, 1.43, and 1.28 R_J. The stellar hosts have masses of 0.94, 1.26, and 1.28 $M_\odot$. Each system shows significant systematic variations in its residual radial velocities, indicating the possible presence of additional components. Based on its Bayesian evidence, the preferred model for HAT-P-44 consists of two planets, including the transiting component, with the outer planet having a period of 872 days, eccentricity of 0.494 ± 0.081, and a minimum mass of 4.0 M_J. Due to aliasing we cannot rule out alternative solutions for the outer planet having a period of 220 days or 438 days. For HAT-P-45, at present there is not enough data to justify the additional free parameters included in a multi-planet model; in this case a single-planet solution is preferred, but the required jitter of 22.5 ± 6.3 m s^{-1} is relatively high for a star of this type. For HAT-P-46 the preferred solution includes a second planet having a period of 78 days and a minimum mass of 2.0 M_J, however the preference for this model over a single-planet model is not very strong. While substantial uncertainties remain as to the presence and/or properties of the outer planetary companions in these systems, the inner transiting planets are well characterized with measured properties that are fairly robust against changes in the assumed models for the outer planets. Continued radial velocity monitoring is necessary to fully characterize these three planetary systems, the properties of which may have important implications for understanding the formation of hot Jupiters.

Key words: planetary systems – stars: individual (HAT-P-44, HAT-P-45, HAT-P-46) – techniques: photometric – techniques: spectroscopic

Online-only material: machine-readable and VO tables

1. INTRODUCTION

There is mounting evidence that systems containing close-in, gas-giant planets (hot Jupiters) are fundamentally different from systems that do not contain such a planet. These differences are seen in the occurrence rate of multiple planets between systems with and without hot Jupiters and in the distribution of projected orbital obliquities[18] of hot Jupiters compared to that of other planets.

Out of the 192 systems listed in the exoplanets orbit database[19] (Wright et al. 2011) containing a planet with $P < 10$ days and $M_p \sin i > 0.1$ M_J, only 5 (2.6%) include confirmed, and well-characterized outer planets (these are υ And, Butler et al. 1997, 1999; HD 217107, Fischer et al. 1999; Vogt et al. 2005; HD 187123, Butler et al. 1998; Wright et al. 2007; HIP 14810, Wright et al. 2007; and HAT-P-13, Bakos et al. 2009). By contrast there are 98 multi-planet systems among the 421 systems (23%) in the database that do not have a hot Jupiter. In addition to the five confirmed multi-planet hot Jupiter systems, there are a number of other hot-Jupiter-bearing systems for which long term trends in their radial velocities (RVs) have been reported. These trends could be due to long-period planetary companions, but their periods are significantly longer than

* Based in part on observations obtained at the W. M. Keck Observatory, which is operated by the University of California and the California Institute of Technology. Keck time has been granted by NOAO (A284Hr) and NASA (N154Hr, N108Hr).
[16] Sloan Fellow.
[17] Packard Fellow.
[18] We use the term obliquity here to refer to the angle between the orbital axis of a planet and the spin axis of its host star.
[19] http://www.exoplanets.org, accessed 2014 January 29.

the time spanned by the observations, and one cannot generally rule out stellar mass companions (a few examples from the Hungarian Automated Telescope Network, or HATNet, survey include HAT-P-7, Pál et al. 2008; HAT-P-17, Howard et al. 2012; Fulton et al. 2013; HAT-P-19, Hartman et al. 2011; and HAT-P-34, Bakos et al. 2012; see also recent results from the "Friends of Hot Jupiters" survey, Knutson et al. 2014). Differences in the occurrence rate of multiple planets between hot-Jupiter-hosting systems and other systems are also apparent from the sample of *Kepler* transiting planet candidates (Latham et al. 2011).

Observations of the Rossiter–McLaughlin effect have revealed that hot Jupiters exhibit a broad range of projected obliquities (e.g., Albrecht et al. 2012). In contrast, the ∼5 multi-planet systems not containing a hot Jupiter, for which the projected obliquity of at least one of the planets has been determined, are all aligned (Albrecht et al. 2013). Differences in the obliquities have been interpreted as indicating different migration mechanisms between the two populations (Sanchis-Ojeda et al. 2012; Albrecht et al. 2013).

There are, however, selection effects which complicate this picture. While most multi-planet systems have been discovered by RV surveys or by the NASA *Kepler* space mission, the great majority of hot Jupiters have been discovered by ground-based transiting planet searches. For the latter surveys access to high-precision RV resources may be scarce, and the candidates are usually several magnitudes fainter than those targeted by RV surveys. To deal with these factors, ground-based transit surveys leverage the known ephemerides of their candidates so as to minimize the number of RV observations needed to detect the orbital variation. In practice this means that many published hot Jupiters do not have the long-term RV monitoring that would be necessary to detect other planetary companions, if present. Moreover, ground-based surveys produce light curves with much shorter time coverage and poorer precision than *Kepler*, so whereas *Kepler* has identified numerous multi-transiting-planet systems, ground-based surveys have not yet discovered any such systems.

In this paper we report the discovery of three new transiting planet systems by the HATNet survey (Bakos et al. 2004). The transiting planets are all classical hot Jupiters, confirmed through a combination of ground-based photometry and spectroscopy, including high-precision RV measurements made with Keck-I/HIRES which reveal the orbital motion of the star about the planet–star center-of-mass. In addition to the orbital motion due to the transiting planets, the RV measurements for all three systems show systematic variations indicating the possible presence of additional planetary-mass components. As we will show, for two of these systems (HAT-P-44 and HAT-P-46) we find that the observations are best explained by multi-planet models, while for the third system (HAT-P-45) additional RV observations would be necessary to claim an additional planet.

In Section 2 we summarize the detection of the photometric transit signal and the subsequent spectroscopic and photometric observations of each star to confirm the planets. In Section 3 we analyze the data to determine the stellar and planetary parameters. Our findings are discussed in Section 4.

2. OBSERVATIONS

The planets presented in this paper were first identified based on data from the HATNet telescopes, and then confirmed through follow-up observations with a variety of ground-based facilities. A general discussions of these procedures are provided in Bakos et al. (2010) and Latham et al. (2009). Here we provide details related to the identification and confirmation of the HAT-P-44, HAT-P-45, and HAT-P-46 systems.

Table 1
Summary of Photometric Observations

Instrument/Field	Date (s)	Number of Images	Cadence (s)	Filter
HAT-P-44				
HAT-5w/G145	2006 Jan–2006 Jul	2880	330	*I* band
HAT-6/G146	2010 Apr–2010 Jul	6668	210	*r* band
KeplerCam	2011 Mar 19	112	134	*i* band
BOS	2011 Apr 14	176	131	*r* band
KeplerCam	2011 Apr 14	85	134	*i* band
KeplerCam	2011 May 27	176	134	*i* band
HAT-P-45				
HAT-5/G432	2010 Sep–2010 Oct	272	330	*r* band
HAT-8/G432	2010 Apr–2010 Oct	7309	210	*r* band
KeplerCam	2011 Apr 02	133	73	*i* band
KeplerCam	2011 Apr 05	44	103	*i* band
FTN	2011 Apr 30	197	50	*i* band
KeplerCam	2011 May 22	174	64	*i* band
KeplerCam	2011 Jun 10	146	64	*i* band
KeplerCam	2011 Jul 05	99	103	*i* band
KeplerCam[a]	2013 May 20	229	50	*g* band
HAT-P-46				
HAT-5/G432	2010 Sep–2010 Oct	300	330	*r* band
HAT-8/G432	2010 Apr–2010 Oct	7633	210	*r* band
KeplerCam	2011 May 05	392	44	*i* band
KeplerCam	2011 May 14	368	49	*i* band
KeplerCam	2011 May 23	247	39	*i* band

Note. [a] This observation was included in the blend analysis of the system, but was not included in the analysis conducted to determine the system parameters.

2.1. Photometric Detection

Table 1 summarizes the HATNet discovery observations of each new planetary system. The HATNet images were processed and reduced to trend-filtered light curves following the procedure described by Bakos et al. (2010). The light curves were searched for periodic box-shaped signals using the Box Least-Squares (BLS; see Kovács et al. 2002) method. Figure 1 shows phase-folded HATNet light curves for HAT-P-44, HAT-P-45, and HAT-P-46 which were selected as showing highly significant transit signals based on their BLS spectra. Cross-identifications, positions, and the available photometry on an absolute scale are provided later in the paper together with other system parameters (Table 10).

We removed the detected transits from the HATNet light curves for each of these systems and searched the residuals for additional transits using BLS, and for other periodic signals using the Discrete Fourier Transform (DFT). Using DFT we do not find a significant signal in the frequency range 0 d^{-1} to 50 d^{-1} in the light curves of any of these systems. For HAT-P-44 we exclude signals with amplitudes above 1.2 mmag, for HAT-P-45 we exclude signals with amplitudes above 1.1 mmag, and for HAT-P-46 we exclude signals with amplitudes above 0.6 mmag. Similarly we do not detect additional transit signals in the light curves of HAT-P-44 or HAT-P-45. For HAT-P-46 we do detect a marginally significant transit signal with a short period of $P = 0.388$ d, a depth of 2.3 mmag, and a S/N in the BLS spectrum of 8.5. The period is neither a harmonic

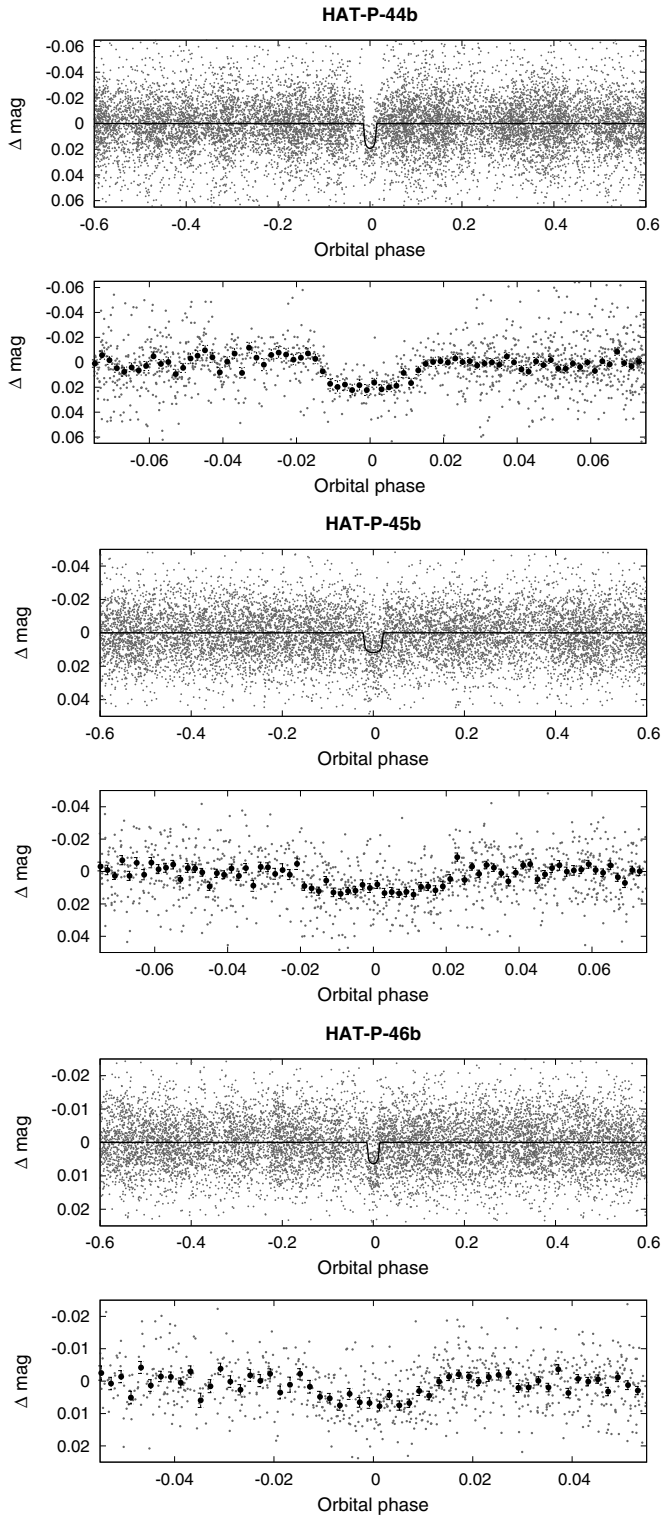

Figure 1. HATNet light curves of HAT-P-44 (top), HAT-P-45 (middle), and HAT-P-46 (bottom). See Table 1 for a summary of the observations. For each planet we show two panels. The top panel shows the unbinned light curve folded with the period resulting from the global fit described in Section 3. The solid line shows the model fit to the light curve (Section 3.4). The bottom panel shows the region zoomed in on the transit. The dark filled circles show the light curve binned in phase with a bin size of 0.002. These are plotted with 1σ uncertainties.

nor an alias of the primary transit signal. Based on our prior experience following up similar signals detected in HATNet light curves we consider this likely to be a false alarm, but mention it here for full disclosure.

Table 2
Summary of Reconnaissance Spectroscopy Observations

Instrument	HJD − 2,400,000	$T_{\rm eff\star}$[a] (K)	$\log g_\star$ (cgs)	$v \sin i$ (km s^{-1})	RV (km s^{-1})
HAT-P-44					
TRES	55557.01323	5250	4.5	2	−34.042
TRES	55583.91926	5250	4.5	2	−34.047
HAT-P-45					
WiFeS	55646.25535	...	...	...	18.9
WiFeS	55648.19634	...	...	...	16.6
WiFeS	55649.24624	...	...	...	18.5
WiFeS	55666.31876	...	...	...	20.1
TRES	55691.96193	6500	4.5	10	23.162
HAT-P-46					
WiFeS	55644.28771	...	...	...	−21.1
WiFeS	55646.25316	...	...	...	−29.6
WiFeS	55647.21574	...	...	...	−21.3
WiFeS	55647.21882	...	...	...	−21.7
WiFeS	55648.17221	...	...	...	−23.9
WiFeS	55649.21348	...	...	...	−25.0
TRES	55659.92299	6000	4.0	6	−21.314
TRES	55728.82463	6000	4.0	6	−21.385

Note. [a] The stellar parameters listed for the TRES observations are the parameters of the theoretical template spectrum used to determine the velocity from the Mg b order. These parameters assume solar metallicity.

2.2. Reconnaissance Spectroscopy

High-resolution, low-S/N "reconnaissance" spectra were obtained for HAT-P-44, HAT-P-45, and HAT-P-46 using the Tillinghast Reflector Echelle Spectrograph (TRES; Fűresz 2008) on the 1.5 m Tillinghast Reflector at FLWO. Medium-resolution reconnaissance spectra were also obtained for HAT-P-45 and HAT-P-46 using the Wide Field Spectrograph (WiFeS) on the ANU 2.3 m telescope at Siding Spring Observatory. The reconnaissance spectroscopic observations and results for each system are summarized in Table 2. The TRES observations were reduced and analyzed following the procedure described by Quinn et al. (2012) and Buchhave et al. (2010), yielding RVs with a precision of ∼50 m s^{-1}, and an absolute velocity zero-point accuracy of ∼100 m s^{-1}. The WiFeS observations were reduced and analyzed as described in Bayliss et al. (2013), providing RVs with a precision of 2.8 km s^{-1}.

Based on the observations summarized in Table 2 we find that all three systems have rms residuals consistent with no significant RV variation within the precision of the measurements (the WiFeS observations of HAT-P-46 have an rms of 3.3 km s^{-1} which is only slightly above the precision determined from observations of RV stable stars). All spectra were single-lined, i.e., there is no evidence that any of these targets consist of more than one star. The gravities for all of the stars indicate that they are dwarfs.

2.3. High Resolution, High S/N Spectroscopy

We obtained high-resolution, high-S/N spectra of each of these objects using HIRES (Vogt et al. 1994) on the Keck-I telescope in Hawaii. The data were reduced to radial velocities in the barycentric frame following the procedure described by Butler et al. (1996). The RV measurements and uncertainties are given in Tables 3–5 for HAT-P-44 through HAT-P-46, respectively. The period-folded data, along with our best fit described below in Section 3, are displayed in Figures 2–4.

Table 3
Relative Radial Velocities, Bisector Spans, and Activity Index Measurements of HAT-P-44

BJD (2,454,000+)	RV[a] ($m\,s^{-1}$)	σ_{RV}[b] ($m\,s^{-1}$)	BS ($m\,s^{-1}$)	σ_{BS} ($m\,s^{-1}$)	S[c]	Phase
1606.11852	113.45	4.35	1.87	7.34	0.131	0.885
1612.12701	4.22	3.65	−9.31	5.29	0.122	0.282
1612.14300	...	...	16.66	7.32	0.134	0.286
1613.03742	77.12	12.22	−56.34	75.72	0.232	0.494
1614.11905	108.82	4.03	0.97	9.57	0.106	0.745
1634.02686	14.58	3.88	−2.67	6.52	0.146	0.374
1663.99061	−3.95	3.76	−3.28	8.67	0.127	0.340
1671.88450	−15.99	4.06	−8.30	7.31	0.115	0.175
1672.95630	12.47	4.01	−11.18	6.83	0.134	0.425
1673.87329	67.10	3.84	12.67	4.49	0.123	0.638
1696.81647	16.79	4.38	31.92	19.95	0.087	0.972
1697.81428	−38.27	3.61	19.79	16.14	0.113	0.204
1698.88909	16.14	6.12	−46.14	50.95	0.211	0.454
1699.79550	27.16	3.65	25.24	12.06	0.141	0.665
1700.84720	7.68	3.34	−0.46	4.24	0.118	0.909
1703.83608	−4.51	3.34	3.70	8.02	0.123	0.604
1704.77501	21.04	3.83	−18.05	12.24	0.123	0.822
1705.79848	−47.96	3.40	−3.55	3.95	0.089	0.060
1707.82993	−17.44	3.90	1.48	6.23	0.137	0.533
1723.83103	−96.08	4.37	−11.27	6.41	0.133	0.253
1945.04563	−1.68	4.68	0.13	19.98	...	0.683
2019.98862	−29.28	4.18	20.91	18.95	...	0.107
2115.75933	−17.99	3.90	27.32	25.83	...	0.373

Notes. Note that for the iodine-free template exposures we do not measure the RV but do measure the BS and S index. Such template exposures can be distinguished by the missing RV value.
[a] The zero point of these velocities is arbitrary. An overall offset γ_{rel} fitted to these velocities in Section 3.4 has *not* been subtracted.
[b] Internal errors excluding the component of astrophysical jitter considered in Section 3.4. The formal errors are likely underestimated in cases where $\sigma_{RV} > 10\ m\,s^{-1}$, as the HIRES Doppler code is not reliable for low S/N observations.
[c] Chromospheric activity index computed as in Isaacson & Fischer (2010).

Table 4
Relative Radial Velocities, Bisector Spans, and Activity Index Measurements of HAT-P-45

BJD (2,454,000+)	RV[a] ($m\,s^{-1}$)	σ_{RV}[b] ($m\,s^{-1}$)	BS ($m\,s^{-1}$)	σ_{BS} ($m\,s^{-1}$)	S[c]	Phase
1668.07265	...	...	−10.44	8.19	0.122	0.213
1696.93207	5.66	7.42	31.53	12.08	0.131	0.436
1697.91247	...	...	40.69	9.05	0.126	0.750
1697.92558	123.23	8.08	38.18	12.38	0.130	0.754
1698.91871	−18.91	7.81	36.59	23.37	0.112	0.071
1699.90750	−74.19	6.89	21.60	22.23	0.117	0.387
1701.10094	97.43	5.92	−29.06	5.82	0.104	0.769
1703.91095	57.59	6.41	−8.91	12.87	0.114	0.667
1705.88887	−128.98	6.28	−0.97	7.20	0.120	0.299
1706.88594	69.84	6.70	5.68	7.63	0.115	0.617
1853.73646	28.34	6.19	−14.06	15.95	...	0.550
2020.03172	124.79	7.60	−4.81	12.64	...	0.696

Notes. Note that for the iodine-free template exposures we do not measure the RV but do measure the BS and S index. Such template exposures can be distinguished by the missing RV value.
[a] The zero point of these velocities is arbitrary. An overall offset γ_{rel} fitted to these velocities in Section 3.4 has *not* been subtracted.
[b] Internal errors excluding the component of astrophysical jitter considered in Section 3.4.
[c] Chromospheric activity index computed as in Isaacson & Fischer (2010).

Table 5
Relative Radial Velocities, Bisector Spans, and Activity Index Measurements of HAT-P-46

BJD (2,454,000+)	RV[a] ($m\,s^{-1}$)	σ_{RV}[b] ($m\,s^{-1}$)	BS ($m\,s^{-1}$)	σ_{BS} ($m\,s^{-1}$)	S[c]	Phase
1696.90831	−3.49	5.78	−1.06	4.36	0.1310	0.008
1696.91767	...	...	15.02	9.27	0.1280	0.010
1697.89794	−60.41	5.22	5.18	4.76	0.1290	0.230
1698.90686	−38.37	5.28	6.22	10.24	0.1510	0.456
1699.89562	−0.43	4.90	2.65	6.29	0.1250	0.677
1703.89107	−24.17	4.57	4.51	7.80	0.1260	0.572
1704.88237	−3.19	5.33	2.11	6.99	0.1240	0.794
1705.87529	−55.16	5.20	−6.74	4.81	0.1270	0.017
1706.87230	−115.33	5.57	−2.18	5.64	0.1270	0.240
1853.71982	−63.30	5.34	−27.87	21.13	...	0.143
1997.09764	20.23	13.90	−27.87	21.13	...	0.268
2113.77814	−87.17	6.61	−22.03	16.45	...	0.411
2195.72876	26.55	5.74	−5.49	14.82	...	0.773

Notes. Note that for the iodine-free template exposures we do not measure the RV but do measure the BS and S index. Such template exposures can be distinguished by the missing RV value.
[a] The zero point of these velocities is arbitrary. An overall offset γ_{rel} fitted to these velocities in Section 3.4 has *not* been subtracted.
[b] Internal errors excluding the component of astrophysical jitter considered in Section 3.4. The formal errors are likely underestimated in cases where $\sigma_{RV} > 10\ m\,s^{-1}$, as the HIRES Doppler code is not reliable for low S/N observations.
[c] Chromospheric activity index computed as in Isaacson & Fischer (2010).

We also show the chromospheric activity S index. The S index for each star was computed following Isaacson & Fischer (2010) and converted to $\log R'_{HK}$ following Noyes et al. (1984). We find median values of $\log R'_{HK} = -5.247 \pm 0.058 \pm 0.10$, $-5.394 \pm 0.072 \pm 0.25$, and $-5.257 \pm 0.036 \pm 0.21$ for HAT-P-44 through HAT-P-46, respectively. The listed uncertainties are the standard errors on the median given the scatter in the individual measurements, followed by the estimated systematic uncertainties assuming an 11% uncertainty in the calibration for S (Isaacson & Fischer 2010). Taken at face value these imply that all three stars are chromospherically quiet. However, since HAT-P-45 is hotter than the $T_{eff} = 6200$ K upper limit over which the Noyes et al. (1984) relation is calibrated, its value should be treated with skepticism. Similarly for HAT-P-46, which has a temperature just below this limit. For HAT-P-44 the low activity index is consistent with the slow projected rotation velocity of $v \sin i = 0.2 \pm 0.5\ km\,s^{-1}$ (see Section 3.1).

Additionally we show the spectral line bisector spans. The bisector spans were computed as in Torres et al. (2007) and Bakos et al. (2007) and show no detectable variation in phase with the RVs, allowing us to rule out various blend scenarios as possible explanations of the observations (see Section 3.2). For HAT-P-45 the bisector spans may be correlated with the residual RVs which may indicate that the jitter for this object is due to stellar activity (see Section 3).

2.4. Photometric Follow-up Observations

Additional photometric observations of each of the transiting planet systems were obtained using the following facilities: the KeplerCam CCD camera on the FLWO 1.2 m telescope, the CCD imager on the 0.8 m remotely operated Byrne Observatory at Sedgwick (BOS) reserve in California, and the Spectral Instrument CCD on the 2.0 m Faulkes Telescope North (FTN) at Haleakala Observatory in Hawaii. Both BOS and FTN are

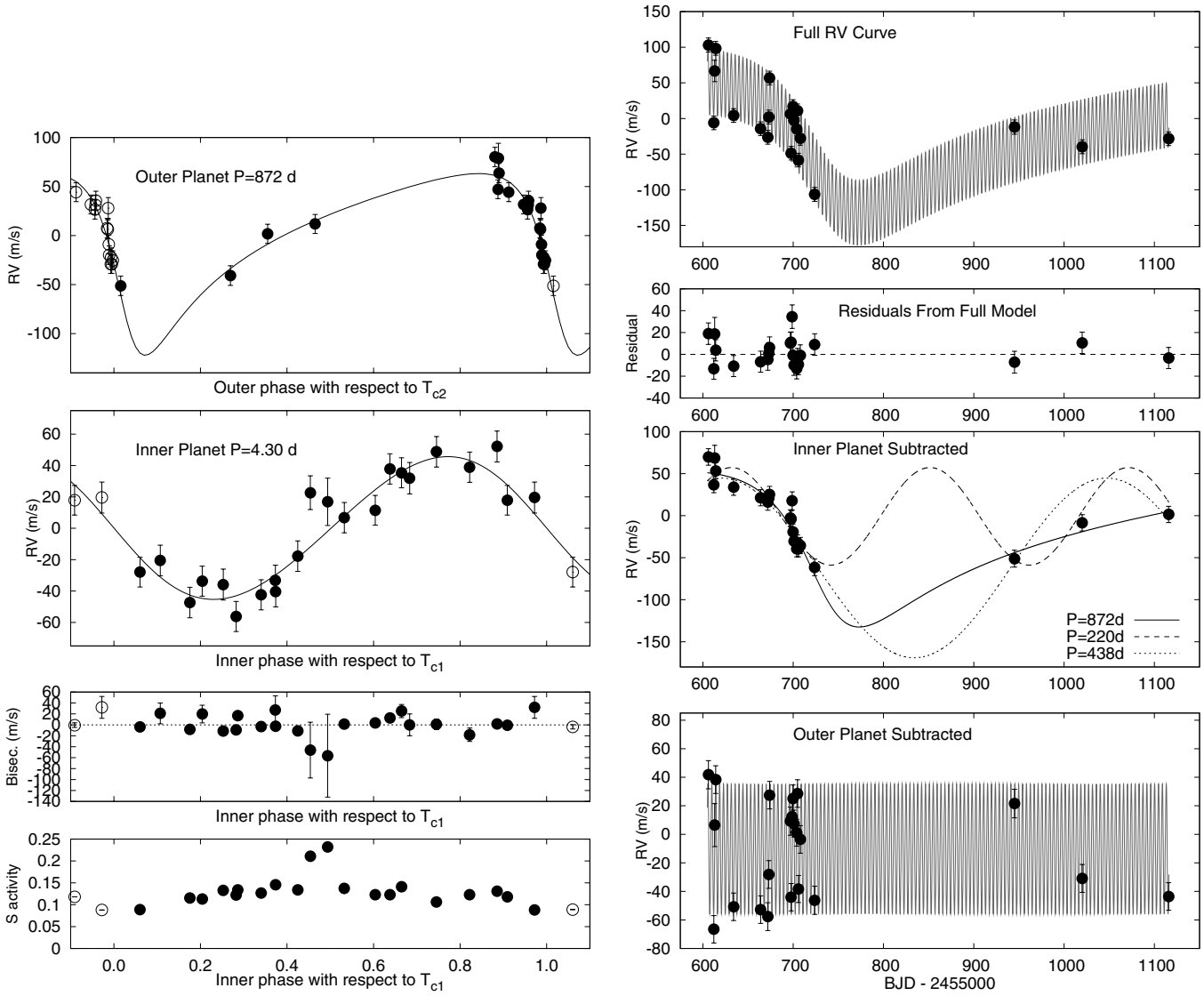

Figure 2. Top left: Keck/HIRES RV measurements for HAT-P-44 shown as a function of orbital phase for the outer planet HAT-P-44c assuming a period of $P = 872$ d, after subtracting off the model orbit for the inner transiting planet HAT-P-44b. Overplotted is our best-fit model (see Table 11). Zero phase corresponds to the time of mid-transit (assuming an edge on orbit; transits of this planet have not been detected). The center-of-mass velocity has been subtracted. Observations shown twice are plotted with open circles. Second left: same as the top left panel, here we show the observations phased using the ephemeris of the transiting planet HAT-P-44b, after subtracting off Keplerian orbit due to HAT-P-44c. Third left: bisector spans (BS), with the mean value subtracted, phased using the ephemeris for the transiting planet. The measurement from the template spectrum is included (see Section 3.2). Bottom left: chromospheric activity index S measured from the Keck spectra, phased using the ephemeris for the transiting planet. Top right: RV curve of HAT-P-44 as a function of time, together with our best-fit two planet model. Second right: RV residuals from the best-fit two-planet model as a function of time. Third right: RV curve of HAT-P-44 as a function of time after subtracting the orbit due to the inner planet HAT-P-44b. For reference, we also show the models for the $P = 220$ days and $P = 438$ days alias signals. Bottom right: RV curve of HAT-P-44 as a function of time after subtracting the orbit due to the outer planet HAT-P-44c. Note the difference in vertical scales for all panels. RV uncertainties in this figure include the jitter which is estimated during the fitting procedure (see Section 3.4.1) and added in quadrature to the formal uncertainties.

operated by the Las Cumbres Observatory Global Telescope (LCOGT; Brown et al. 2013). The observations for each target are summarized in Table 1.

The reduction of the KeplerCam images was performed using the aperture photometry procedure described by Bakos et al. (2010). The BOS and FTN observations were reduced in a similar manner. The resulting differential light curves were further filtered using the External Parameter Decorrelation (EPD) and Trend Filtering Algorithm (TFA)[20] methods applied simultaneously with light curve modeling so that uncertainties in the noise filtering process contribute to the uncertainties on the physical parameters (for more details, see Bakos et al. 2010). The light curves, and best-fit models, are shown in Figures 5–7 for HAT-P-44 through HAT-P-46, respectively; the individual measurements are reported in Tables 6–8.

[20] EPD and TFA both involve fitting the light curve as a linear combination of trend basis vectors. The EPD vectors are a set of light curve specific signals, such as the hour angle of the observations and the FWHM of the point-spread function (PSF). The TFA vectors are the differential light curves of a carefully selected sample of comparison stars in the same field of view as the target.

3. ANALYSIS

3.1. Properties of the Parent Star

Stellar atmospheric parameters for each star were measured using the Spectroscopy Made Easy (SME; Valenti & Piskunov 1996) and the Valenti & Fischer (2005) atomic line database.

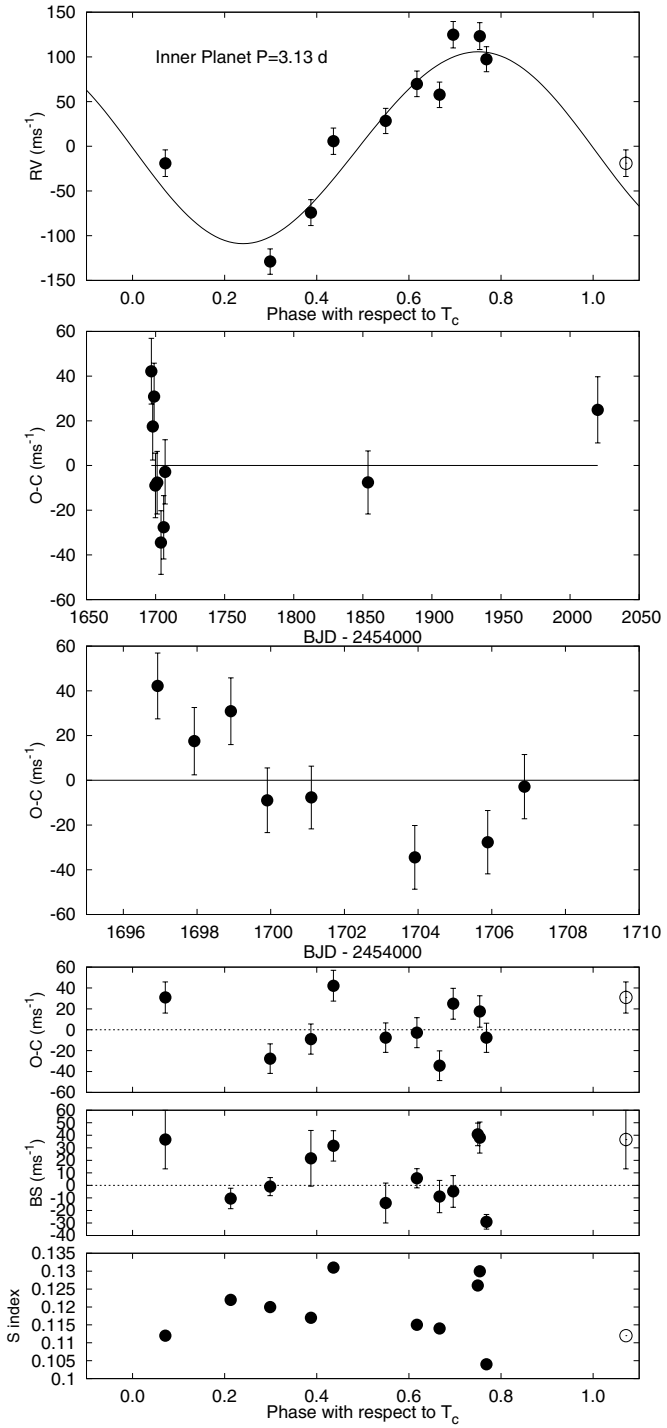

Figure 3. Top panel: Keck/HIRES RV measurements for HAT-P-45 shown as a function of orbital phase, along with our best-fit single-planet model (see Table 13). Zero phase corresponds to the time of mid-transit. The center-of-mass velocity has been subtracted. Second panel: velocity $O-C$ residuals from the best fit shown as a function of time. Third panel: same as the second panel, here we zoom in on the residuals for the first eight observations. Fourth panel: velocity *O–C* residuals shown as a function of orbital phase. Fifth panel: bisector spans (BS), with the mean value subtracted. The measurement from the template spectrum is included (see Section 3.2). Bottom panel: chromospheric activity index S measured from the Keck spectra. Note the different vertical scales of the panels. Observations shown twice are represented with open symbols.

We analyzed the Keck/HIRES template spectra for each star, which yielded the following *initial* values and uncertainties.

1. *HAT-P-44*—effective temperature $T_{\rm eff\star} = 5295 \pm 100$ K, metallicity [Fe/H] $= 0.33 \pm 0.1$ dex, stellar surface gravity $\log g_\star = 4.42 \pm 0.1$ (cgs), and projected rotational velocity $v \sin i = 0.2 \pm 0.5$ km s^{-1}.
2. *HAT-P-45*—effective temperature $T_{\rm eff\star} = 6270 \pm 100$ K, metallicity [Fe/H] $= 0.03 \pm 0.1$ dex, stellar surface gravity $\log g_\star = 4.26 \pm 0.1$ (cgs), and projected rotational velocity $v \sin i = 9.0 \pm 0.5$ km s^{-1}.
3. *HAT-P-46*—effective temperature $T_{\rm eff\star} = 6280 \pm 100$ K, metallicity [Fe/H] $= 0.38 \pm 0.1$ dex, stellar surface gravity $\log g_\star = 4.38 \pm 0.1$ (cgs), and projected rotational velocity $v \sin i = 4.5 \pm 0.5$ km s^{-1}.

These values were used to determine initial values for the limb-darkening coefficients, which we fix during the light curve modeling (Section 3.4). This modeling, when combined with the Yonsei-Yale (YY) theoretical stellar evolution models (Yi et al. 2001), provides a refined determination of the stellar surface

Table 6
High-precision Differential Photometry of HAT-P-44

BJD (2,400,000 +)	Mag[a]	$\sigma_{\rm Mag}$	Mag(orig)[b]	Filter
55640.84396	−0.00143	0.00122	12.01460	*i*
55640.84597	0.00034	0.00119	12.01570	*i*
55640.84767	−0.00081	0.00119	12.01670	*i*
55640.84922	0.00007	0.00122	12.01650	*i*
55640.85109	−0.00137	0.00119	12.01450	*i*
55640.85271	0.00200	0.00122	12.01870	*i*
55640.85427	−0.00050	0.00121	12.01580	*i*
55640.85593	−0.00410	0.00122	12.01310	*i*
55640.85747	−0.00288	0.00122	12.01370	*i*
55640.85902	−0.00104	0.00119	12.01550	*i*

Notes.
[a] The out-of-transit level has been subtracted. These magnitudes have been subjected to the EPD and TFA procedures, carried out simultaneously with the transit fit.
[b] Raw magnitude values without application of the EPD and TFA procedures.

(This table is available in its entirety in machine-readable and Virtual Observatory (VO) forms in the online journal. A portion is shown here for guidance regarding its form and content.)

Table 7
High-precision Differential Photometry of HAT-P-45

BJD (2,400,000 +)	Mag[a]	$\sigma_{\rm Mag}$	Mag(orig)[b]	Filter
55654.89724	0.01314	0.00112	11.34410	*i*
55654.89809	0.01315	0.00112	11.34380	*i*
55654.89894	0.01560	0.00112	11.34390	*i*
55654.89981	0.01522	0.00112	11.34580	*i*
55654.90065	0.01456	0.00113	11.34380	*i*
55654.90152	0.01758	0.00112	11.34740	*i*
55654.90235	0.01425	0.00112	11.34350	*i*
55654.90322	0.01632	0.00112	11.34700	*i*
55654.90407	0.01552	0.00113	11.34650	*i*
55654.90491	0.01267	0.00112	11.34330	*i*

Notes.
[a] The out-of-transit level has been subtracted. These magnitudes have been subjected to the EPD and TFA procedures, carried out simultaneously with the transit fit.
[b] Raw magnitude values without application of the EPD and TFA procedures.

(This table is available in its entirety in machine-readable and Virtual Observatory (VO) forms in the online journal. A portion is shown here for guidance regarding its form and content.)

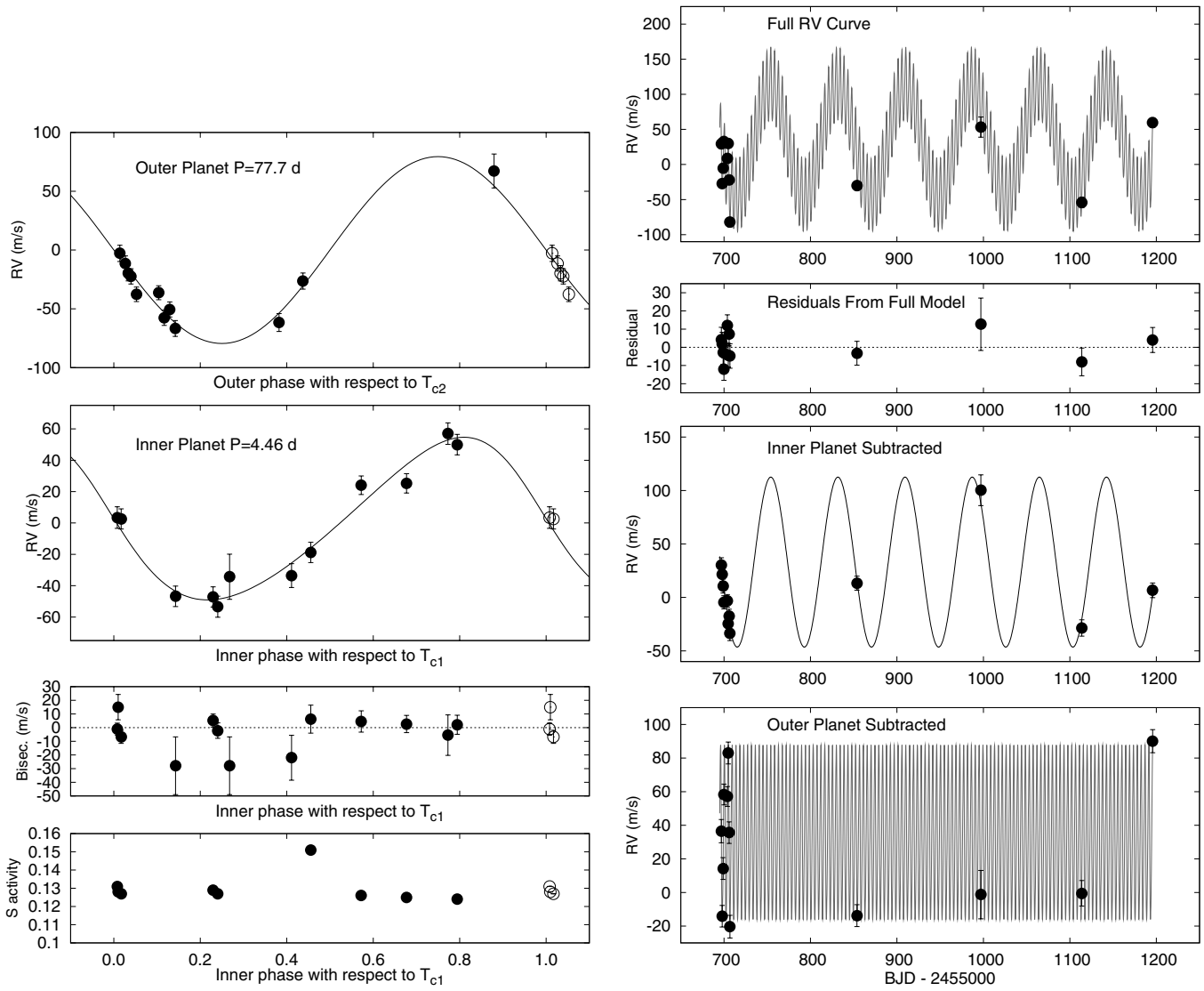

Figure 4. Keck/HIRES observations of HAT-P-46. The panels are as in Figure 2. The parameters used in the best-fit model are given in Table 13.

Table 8
High-precision Differential Photometry of HAT-P-46

BJD (2,400,000 +)	Mag[a]	$\sigma_{\rm Mag}$	Mag(orig)[b]	Filter
55687.79447	−0.00440	0.00112	10.45700	*i*
55687.79497	0.00288	0.00113	10.46460	*i*
55687.79596	−0.00087	0.00113	10.46190	*i*
55687.79647	−0.00065	0.00113	10.46210	*i*
55687.79699	−0.00327	0.00112	10.45850	*i*
55687.79749	0.00222	0.00112	10.46330	*i*
55687.79798	0.00089	0.00113	10.46300	*i*
55687.79850	−0.00339	0.00112	10.45840	*i*
55687.79901	0.00378	0.00112	10.46610	*i*
55687.79952	0.00308	0.00113	10.46470	*i*

Notes.
[a] The out-of-transit level has been subtracted. These magnitudes have been subjected to the EPD and TFA procedures, carried out simultaneously with the transit fit.
[b] Raw magnitude values without application of the EPD and TFA procedures.

(This table is available in its entirety in machine-readable and Virtual Observatory (VO) forms in the online journal. A portion is shown here for guidance regarding its form and content.)

gravity (Sozzetti et al. 2007) which we then fix in a second SME analysis of the spectra yielding our adopted atmospheric parameters. For HAT-P-44 the revised surface gravity is close enough to the initial SME value that we do not conduct a second SME analysis. The final adopted values of $T_{\rm eff\star}$, [Fe/H], and $v \sin i$ are listed for each star in Table 10. We compare the measured $a/R_\star$ and $T_{\rm eff\star}$ values for each star to the YY model isochrones in Figure 8.

The values of $\log g_\star$, as well as of properties inferred from the evolution models (such as the stellar masses and radii) depend on the eccentricity and semi-amplitude of the transiting planet's orbit, which in turn depend on how the RV data are modeled. In modeling these data we varied the number of planets considered for a given system, and whether or not these planets are fixed to circular orbits. Although $T_{\rm eff\star}$, [Fe/H], and $v \sin i$ will also depend on the fixed value of $\log g_\star$ we found generally that $\log g_\star$ did not change enough between the models that provide a good fit to the data to justify carrying out a separate SME analysis using the $\log g_\star$ value determined from each model. As we discuss in Section 3.4.2 we tested numerous models; our final adopted values for these model-dependent parameters are presented in that section.

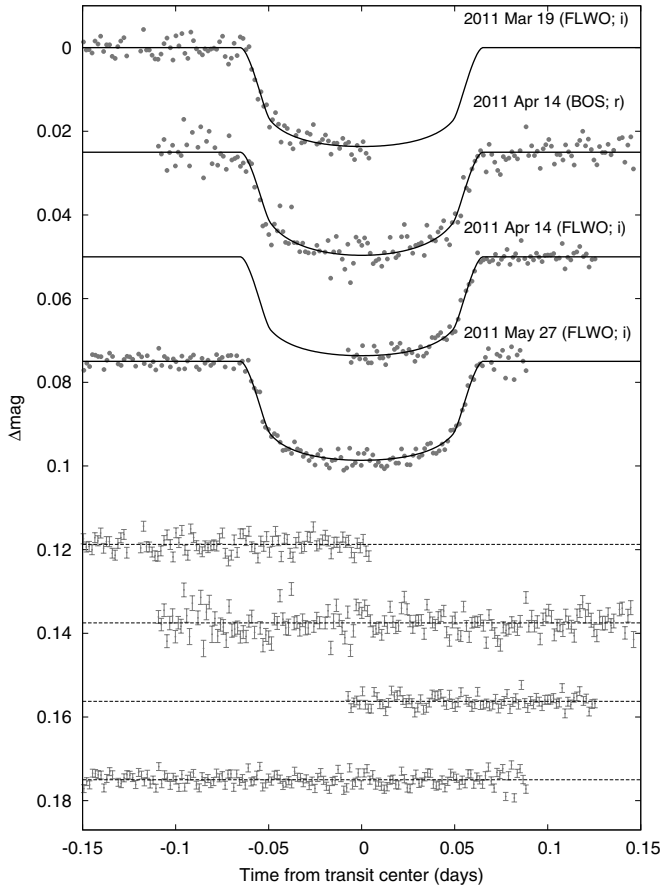

Figure 5. Unbinned transit light curves for HAT-P-44. The light curves have been EPD and TFA processed, as described in Section 3.4. The dates of the events, the facilities used to collect the light curves, and the filters used are indicated. Curves after the first are displaced vertically for clarity. Our best fit from the global modeling described in Section 3.4 is shown by the solid lines. Residuals from the fits are displayed at the bottom, in the same order as the top curves. The error bars represent the photon and background shot noise, plus the readout noise.

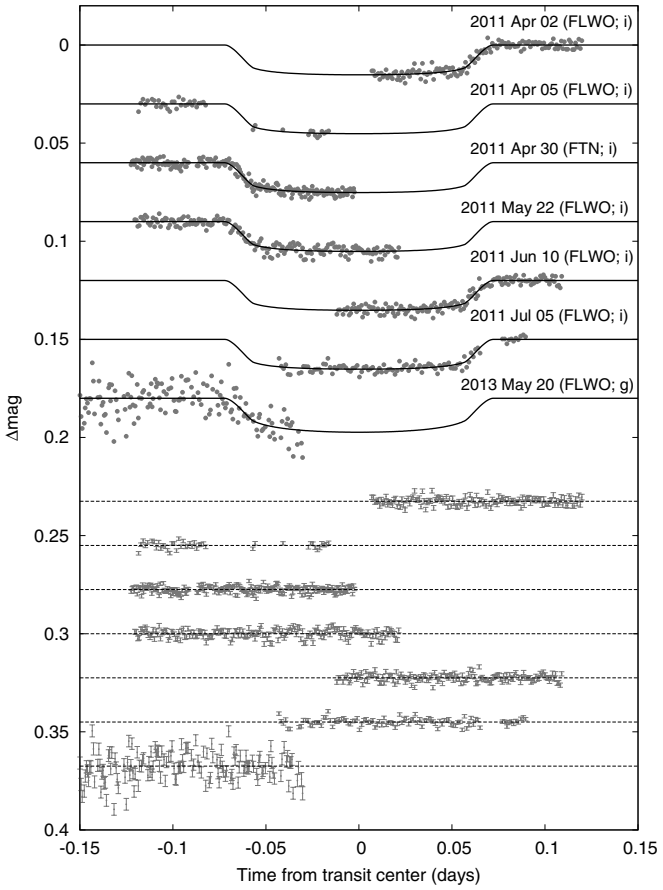

Figure 6. Similar to Figure 5; here we show the follow-up light curves for HAT-P-45. The *g*-band light curve obtained on 2013 May 20 was used for rejecting blend scenarios but was not used in determining the system parameters as the analysis was performed prior to carrying out this observation.

We determine the distance and extinction to each star by comparing the J, H, and K_S magnitudes from the 2MASS Catalogue (Skrutskie et al. 2006), and the V and I_C magnitudes from the TASS Mark IV Catalogue (Droege et al. 2006), to the expected magnitudes from the stellar models. We use the transformations by Carpenter (2001) to convert the 2MASS magnitudes to the photometric system of the models (ESO), and use the Cardelli et al. (1989) extinction law, assuming a total-to-selective extinction ratio of $R_V = 3.1$, to relate the extinction in each bandpass to the V-band extinction A_V. The resulting A_V and distance measurements are given with the other model-dependent parameters. We find that HAT-P-44 is not significantly affected by extinction, consistent with the Schlegel et al. (1998) dust maps which yield a total extinction of $A_V = 0.038$ mag along the line of sight to HAT-P-44. HAT-P-45 and HAT-P-46, on the other hand, have low Galactic latitudes ($b = 6.^\circ0$ and $b = 9.^\circ6$, respectively), and are significantly affected by extinction. We find $A_V = 1.900 \pm 0.169$ mag and $A_V = 0.832 \pm 0.145$ mag for our preferred models for HAT-P-45 and HAT-P-46, respectively. For comparison, the Schlegel et al. (1998) maps yield a *total* line of sight extinction of $A_V = 5.89$ mag and $A_V = 3.25$ mag for HAT-P-45 and HAT-P-46, respectively, or $A_V \sim 0.8$ mag to both sources after applying the distance and excess extinction corrections given by Bonifacio et al. (2000). At these low Galactic latitudes the extinction estimates based on the Schlegel et al. (1998) dust maps are not reliable, so the discrepancy between the dust-map-based and photometry-based A_V estimates for HAT-P-45 is not unexpected. After correcting for extinction the measured and expected photometric color indices are consistent for each star.

3.2. Excluding Blend Scenarios

To rule out the possibility that any of these objects might be a blended stellar eclipsing binary system we carried out a blend analysis as described in Hartman et al. (2012).

We find that for HAT-P-44 we can exclude most blend models, consisting either of a hierarchical triple star system, or a blend between a background eclipsing binary and a foreground bright star, based on the light curves. Those models that cannot be excluded with at least 5σ confidence would have been detected as obviously double-lined systems, showing many km s^{-1} RV and BS variations.

For HAT-P-45 and HAT-P-46 the significant reddening (Section 3.1) allows a broader range of blend scenarios to fit the photometric data. For a system like HAT-P-44, where there is no significant reddening and the available calibrated broad-band photometry agrees well with the spectroscopically determined temperature, the calibrated photometry places a strong constraint on blend scenarios where the two brightest stars in the blend have different temperatures. For HAT-P-45 and HAT-P-46, on the other hand, such blends can be accommodated by reducing the reddening in the fit. Indeed we find for both

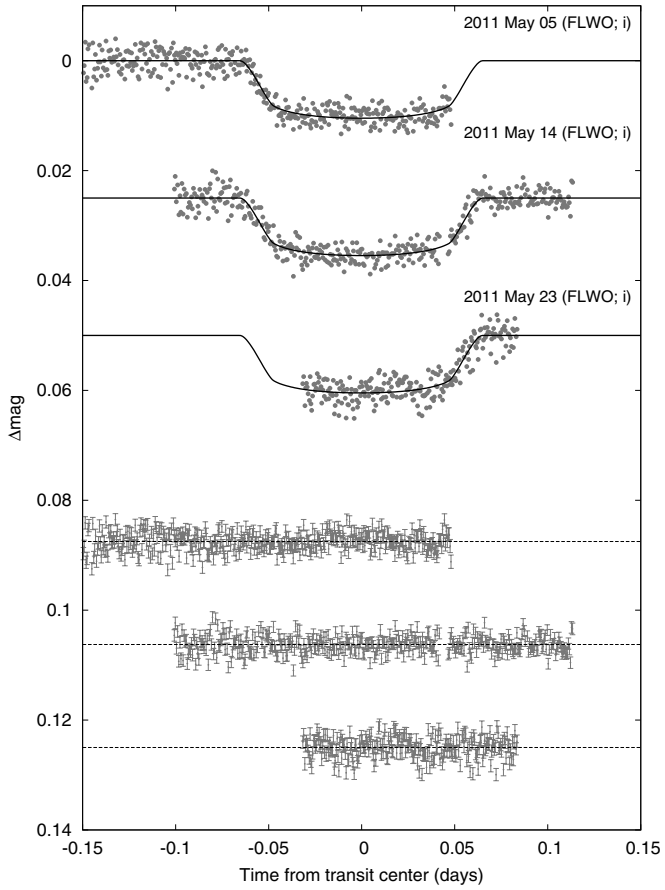

Figure 7. Similar to Figure 5; here we show the follow-up light curves for HAT-P-46.

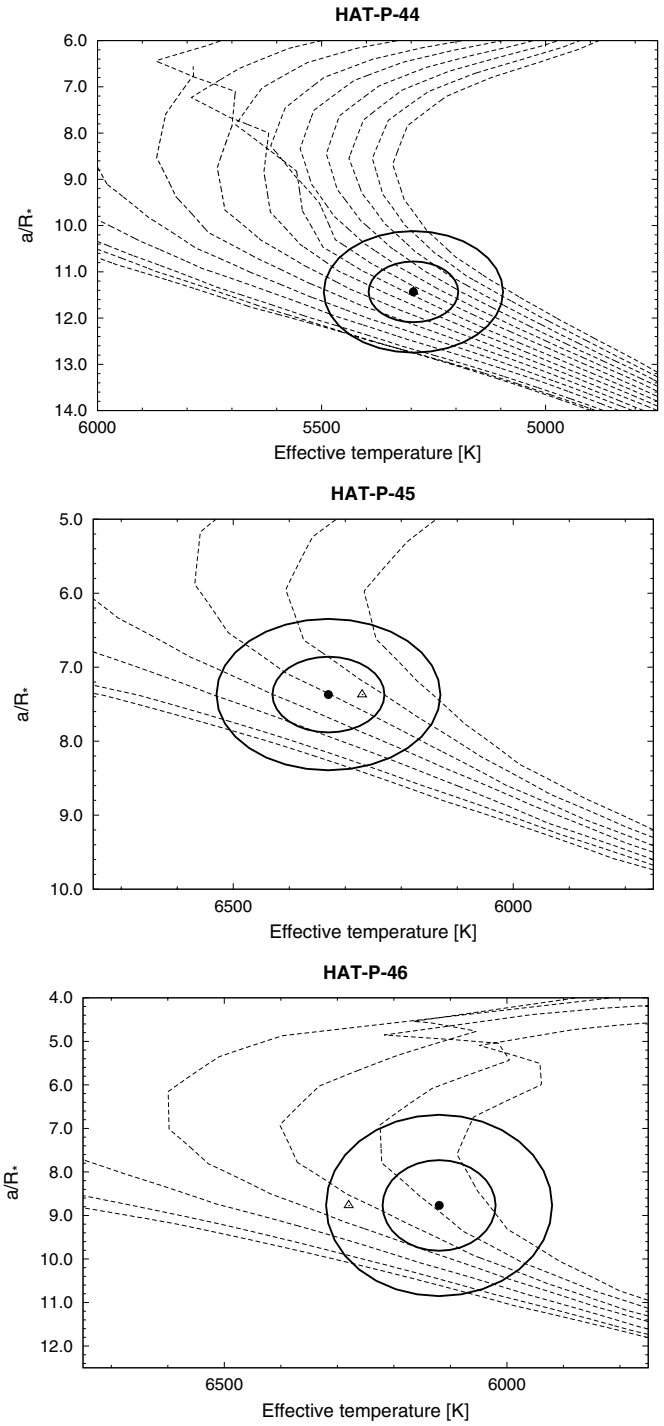

Figure 8. Model isochrones from Yi et al. (2001) for the metallicities of HAT-P-44 (top), HAT-P-45 (center), and HAT-P-46 (bottom). For HAT-P-44 the isochrones are shown for ages of 0.2 Gyr, 0.6 Gyr, and 1.0 Gyr to 13.0 Gyr in steps of 1.0 Gyr (left to right), while for HAT-P-44 and HAT-P-45 the isochrones are shown for ages of 0.2 Gyr, and 0.5 Gyr to 3.0 Gyr in steps of 0.5 Gyr (left to right). The adopted values of $T_{\rm eff\star}$ and $a/R_\star$ are shown together with their 1σ and 2σ confidence ellipsoids. For HAT-P-45 and HAT-P-46 the initial values of $T_{\rm eff\star}$ and $a/R_\star$ from the first SME and light curve analyses are represented with a triangle.

HAT-P-45 and HAT-P-46 that the calibrated broadband photometry are fit slightly better by models that incorporate multiple stars (blends) together with reddening, than by a model consisting of only a single reddened star. The difference between these models is small enough, however, that we do not consider this improvement to be significant; such differences may be due to the true extinction law along this line of sight being slightly different from our assumed $R_V = 3.1$ Cardelli et al. (1989) extinction law.

To better constrain the possible blend scenarios we obtained a partial g band light curve for HAT-P-45 using Keplercam on the night of 2013 May 20. The photometry was reduced as described in Section 2.4 and included in our blend analysis procedure. We show this light curve in Figure 6, though we note that it was not included in the planet parameter determination which was carried out prior to these observations. Even though it is only a partial event, this light curve significantly restricts the range of blends that can explain the photometry for HAT-P-45, excluding scenarios that predict substantially different g and i band transit depths.

Although the broadband photometry permits a wide range of possible blend scenarios, for both HAT-P-45 and HAT-P-46 the nonplanetary blend scenarios which fit the photometric data can be ruled out based on the BS and RV variations. For HAT-P-45 we find that blend scenarios that fit the photometric data (scenarios that cannot be rejected with $>5\sigma$ confidence) yield several km s^{-1} BS and RV variations, whereas the actual BS rms is 24 m s^{-1}. Without the g band light curve for HAT-P-45 some of the blend scenarios consistent with the photometry for this system predict BS and RV variations only slightly in excess of what was measured, illustrating the importance of this light curve. For HAT-P-46 the blend scenarios that fit the photometric data would result in BS variations with rms $>$ 80 m s^{-1}, much greater than the measured scatter of 14 m s^{-1}.

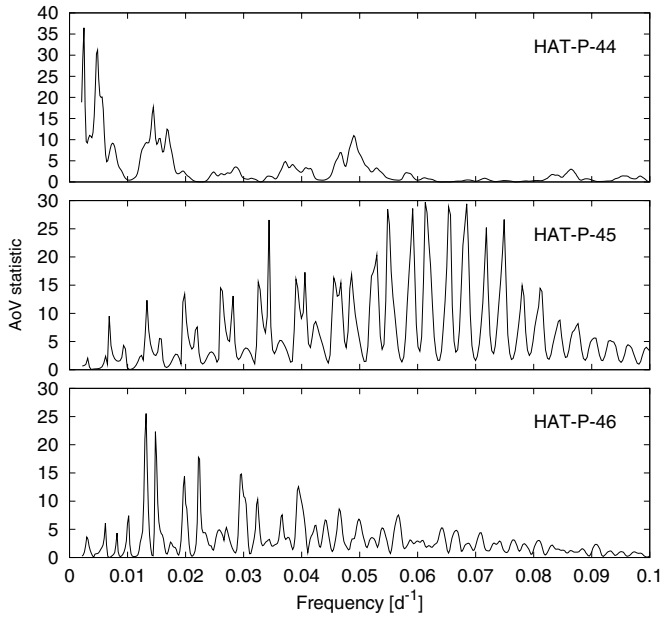

Figure 9. Harmonic AoV periodograms of the RV residuals from the best-fit single planet models for HAT-P-44, HAT-P-45, and HAT-P-46.

We conclude that for all three objects the photometric and spectroscopic observations are best explained by transiting planets. We are not, however, able to rule out the possibility that any of these objects is actually a composite stellar system with one component hosting a transiting planet. Given the lack of definite evidence for multiple stars we analyze all of the systems assuming only one star is present in each case. If future observations identify the presence of stellar companions, the planetary masses and radii inferred in this paper will require moderate revision (e.g., Adams et al. 2013).

3.3. Periodogram Analysis of the RV Data

For each object initial attempts to fit the data as a single planet system following the method described in Section 3.4 yielded an exceptionally high χ^2 per degree of freedom (80.5, 19.7, and 23.0 for the full RV data of HAT-P-44, HAT-P-45, and HAT-P-46, respectively). Inspection of the RV residuals showed systematic variations (linear or quadratic in time) suggestive of additional components. We therefore continued to collect RV observations with Keck/HIRES for each of the objects. In all three cases the new RVs did not continue to follow the previously identified trends.

Figure 9 shows the harmonic Analysis of Variance (AoV) periodograms (Schwarzenberg-Czerny 1996) of the residual RVs from the best-fit single-planet model for each system.[21] In each case strong aliasing gives rise to numerous peaks in the periodograms which could potentially phase the residual data; we are thus not able to identify a unique period for the putative outer companions in any of these systems.

For HAT-P-44 the two highest peaks are at $f = 0.0023626\,\mathrm{day}^{-1}$ ($P = 423.26$ days) and $f = 0.0044477\,\mathrm{day}^{-1}$ ($P = 224.83$ days), with false alarm probabilities of $\sim 2.5 \times 10^{-5}$ and 3.3×10^{-4}, respectively. The periodogram of the residuals of a model consisting of the transiting planet and a planet with $P \sim 220$ days (when fitting the data simultaneously for two planets this model provides a slightly better fit than when the outer planet has a period of $P = 423$ days) yields a peak at $P = 17.7$ days with a false alarm probability of 0.16. Alias peaks are also seen at $P = 17.3$ days, $P = 18.6$ days, $P = 11.4$ days, $P = 11.7$ days, $P = 13.3$ days, and several other values with decreasing significance.

For HAT-P-45 a number of frequencies are detected in the periodogram of the RV residuals from the best-fit single-planet model. These periods are all aliases of each other. The highest peak is at $f = 0.065289\ \mathrm{day}^{-1}$ ($P = 15.316$ days), with a false alarm probability of $\sim 10^{-2}$. For HAT-P-46 the two highest peaks are at $f = 0.012977\ \mathrm{day}^{-1}$ ($P = 77.061$ days) and $f = 0.014708\ \mathrm{day}^{-1}$ ($P = 67.988$ days), each with false alarm probabilities of $\sim 10^{-2}$ (or $\sim 10^{-4}$ if uniform uncertainties are adopted as discussed further below).

The false alarm probabilities given above include a correction for the so-called "bandwidth penalty" (i.e., a correction for the number of independent frequencies that are tested by the periodogram); here we restricted the search to a frequency range of $0.02\ \mathrm{day}^{-1} < f < 0.2\ \mathrm{day}^{-1}$ and used the Horne & Baliunas (1986) approximation to estimate the number of independent frequencies tested (the resulting false alarm probability may be inaccurate by as much as a factor of ~ 10). Note that adopting a broader frequency range for the periodograms (e.g., up to the Nyquist limit, which for the HAT-P-44 data would be $\sim 250\ \mathrm{day}^{-1}$) significantly increases the false alarm probabilities. We expect, however, that systems containing multiple Jupiter-mass planets with orbital periods less than 5 days would be dynamically unstable, allowing us to restrict the frequency range to consider on physical grounds.

For HAT-P-44 and HAT-P-45 the false alarm probabilities are approximately the same for high jitter as they are when the jitter is set to 0. For HAT-P-46 the false alarm probabilities are smaller when the errors are dominated by jitter (10^{-4} with jitter versus 10^{-2} without jitter).

3.4. Global Model of the Data

We modeled simultaneously the HATNet photometry, the follow-up photometry, and the high-precision RV measurements using a procedure similar to that described in detail by Bakos et al. (2010) with modifications described by Hartman et al. (2012). For each system we used a Mandel & Agol (2002) transit model, together with the EPD and TFA trend-filters, to describe the follow-up light curves, a Mandel & Agol (2002) transit model for the HATNet light curve(s), and a Keplerian orbit using the formalism of Pál (2009) for the RV curve. A significant change that we have made compared to the analysis conducted in our previous discovery papers was to include the RV jitter as a free parameter in the fit, which we discuss below. We then discuss our methods for distinguishing between competing classes of models used to fit the data, and comment on the orbital stability of potential models.

3.4.1. RV Jitter

It is well known that high-precision RV observations of stars show non-periodic variability in excess of what is expected based on the measurement uncertainties. This "RV jitter" depends on properties of the star including the effective temperature of its photosphere, its chromospheric activity, and the projected equatorial rotation velocity of the star (see Wright 2005; Isaacson & Fischer 2010, who discuss the RV jitter from Keck/HIRES measurements). In most exoplanet studies the typical

[21] Using alternative methods, such as the Discrete Fourier Transform, the Lomb-Scargle periodogram, or a $\Delta\chi^2$ periodogram, yield similar frequencies, but the false alarm probabilities differ between the methods due to differences in the statistics adopted.

method for handling this jitter has been to add it in quadrature to the measurement uncertainties, assuming that the jitter is Gaussian white noise. One then either adopts a jitter value that is found to be typical for similar stars, or chooses a jitter such that χ^2 per degree of freedom is unity for the best-fit model. In our previous discovery papers we adopted the latter approach.

When testing competing models for the RV data the jitter is an important parameter—the greater the jitter the smaller the absolute χ^2 difference between two models, and the less certain one can be in choosing one over the other. Both of the typical approaches for handling the jitter have shortcomings: the former does not allow for the possibility that a star may have a somewhat higher (or lower) than usual jitter, while the latter ignores any prior information that may be used to disfavor jitter values that would be very unusual. An alternative approach is to treat the jitter as a free parameter in the fit, but use the empirical distribution of jitters as a prior constraint.

The method of allowing the jitter to vary in an MCMC analysis of an RV curve was previously adopted by Gregory (2005). As was noted in that work, when allowing terms which appear in the uncertainties to vary in an MCMC fit, the logarithm of the likelihood is no longer simply $\ln L = -\chi^2/2 + C$ where C is a normalization constant that is independent of the parameters, and can be ignored for most applications. Instead one should use $\ln L = -\chi^2/2 + \sum_{i=1}^{N} \ln(1/e_i) + C$, where e_i is the error for measurement i and in this case is given by $e_i = \sqrt{\sigma_i^2 + \sigma_{\rm jitter}^2}$ for formal uncertainty σ_i and jitter $\sigma_{\rm jitter}$. When the uncertainties do not include free parameters, the term $\sum_{i=1}^{N} \ln(1/e_i)$ is constant, and included in C.

The analysis by Gregory (2005) used an uninformative prior on the jitter, which effectively forces the jitter to the value that results in $\chi^2/{\rm dof} = 1$; here we make use of the empirical jitter distribution found by Wright (2005) to set a prior on the jitter. Wright (2005) provides the distributions for stars in a several bins separated by $B - V$, activity, and luminosity above the main sequence. The histograms appear to be well-matched by log-normal distributions of the form:

$$P(\sigma_{\rm jitter})d\sigma_{\rm jitter} = \frac{1}{\sigma_{\rm jitter}\sqrt{2\pi\bar{\sigma}^2}} e^{-\frac{(\ln\sigma_{\rm jitter} - \bar{\mu})^2}{2\bar{\sigma}^2}} d\sigma_{\rm jitter}. \quad (1)$$

Figure 10 compares this model to the jitter histograms. For HAT-P-44, which falls in the low-activity bin with $\Delta M_v < 1$ and $0.6 < B - V < 1.4$, we find $\bar{\sigma} = 0.496$, $\bar{\mu} = 1.251$, with $\sigma_{\rm jitter}$ measured in units of m s^{-1}. For HAT-P-45 and HAT-P-46, which fall in the bin of low-activity stars with $\Delta M_V < 1$ and $B - V < 0.6$, we find $\bar{\sigma} = 0.688$, and $\bar{\mu} = 1.419$.

The posterior probability density for the parameters θ, given the data D and model M is given by Bayes' relation:

$$P(\theta|D, M) = \frac{P(\theta|M)P(D|\theta, M)}{P(D|M)} \quad (2)$$

which in our case takes the form:

$$P(\theta|D, M) = C\exp(\ln L + \ln P(\theta|M))$$
$$= C\exp(-\chi^2/2 + \sum_{i=1}^{N} \ln(1/e_i) + \ln P(\sigma_{\rm jitter}))$$

where C represents constants that are independent of θ (note we adopt uniform priors on all jump parameters other than $\sigma_{\rm jitter}$). We use a differential evolution MCMC procedure (ter Braak 2006; Eastman et al. 2013) to explore this distribution.

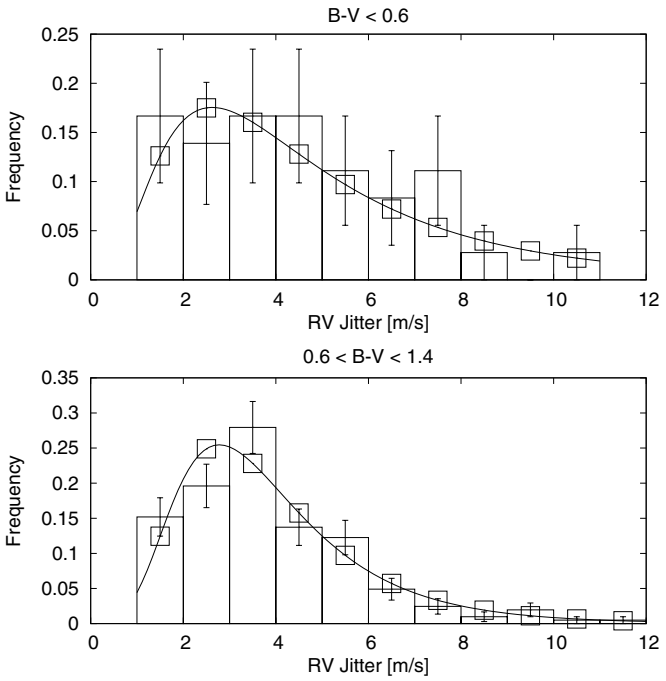

Figure 10. Comparison of the distribution of Keck/HIRES jitter values for low activity main sequence stars taken from Wright (2005) to our model distributions. The histograms show the empirical distributions with Poisson error bars, the open squares show Equation (1) integrated over each bin, and the solid curves are included to show the form of the distribution. The top panel is for stars with $B - V < 0.6$, appropriate for HAT-P-45 and HAT-P-46, the bottom panel is for stars with $0.6 < B - V < 1.4$, appropriate for HAT-P-44.

3.4.2. Model Selection

As discussed in the previous subsection, modeling these objects as single-planet systems yields RV residuals with large scatter and evidence of long-term variations. We also attempted fitting the data for HAT-P-44 and HAT-P-46 including linear or quadratic trends in addition to the single-planet systems, but found that these models do not provide good fits to the data. We therefore performed the analysis of each system including additional Keplerian components in their RV models.

We use the Bayes Factor to select between these competing models; here we describe how this is computed. The Bayesian evidence Z is defined by

$$Z = P(D|M) = \int d\theta\, P(\theta|M)P(D|\theta, M) \quad (3)$$

where $P(D|M)$ is the probability of observing the data D given the model M, marginalized over the model parameters θ. The Bayes factor $K_{1,2}$ comparing the posterior probabilities for models M_1 and M_2 given the data D is defined by

$$K_{1,2} = \frac{P(M_1|D)}{P(M_2|D)} = \frac{P(M_1)P(D|M_1)}{P(M_2)P(D|M_2)} \quad (4)$$

where $P(M)$ is the prior probability for model M. Assuming equal priors for the different models tested, the Bayes factor is then equal to the evidence ratio:

$$K_{1,2} = \frac{Z_1}{Z_2}. \quad (5)$$

If $K_{1,2} > 1$ then model M_1 is favored over model M_2.

In practice Z is difficult to determine as it requires integrating a complicated function over a high-dimensional space (e.g.,

Feroz et al. 2009). Recently, however, Weinberg et al. (2013) have suggested a simple and relatively accurate method for estimating Z directly from the results of an MCMC simulation. Their method involves using the MCMC results to identify a small region of parameter space with high posterior probability, numerically integrating over this region, and applying a correction to scale the integral from the subregion to the full parameter space. The correction is determined from the posterior parameter distribution estimated as well from the MCMC. We use this method to estimate Z and K for each model. However, for practical reasons we use the MCMC sample itself to conduct a Monte Carlo integration of the parameter subregion, rather than following the suggested method of using a uniform resampling of the subregion. As shown by Weinberg et al. (2013) the method that we follow provides a somewhat biased estimate of Z, with errors in $\ln Z \lesssim 0.5$. For this reason we do not consider $\ln Z$ differences between models that are <1 to be significant.

In Table 9 we list the models fit for each system, and provide estimates of the Bayes Factors for each model relative to a fiducial model of a single transiting planet on an eccentric orbit. For reference we also provide the Bayesian Information Criterion (BIC) estimator for each model, which is given by

$$\mathrm{BIC} = -2 \ln L_{\max} + N_{\mathrm{p}} \ln N_{\mathrm{d}} \quad (6)$$

for a model with N_{p} free parameters fit to N_{d} data points yielding a maximum likelihood of $L_{\max}$. The BIC is determined solely from the highest likelihood value, making it easier to calculate than K. Models with lower BIC values are generally favored. Note, however, that the BIC is a less accurate method for distinguishing between models than is K. We also provide, for reference, the Bayes Factors determined when the jitter of each system is fixed to a typical value throughout the analysis.

3.5. Resulting Parameters

The planet and stellar parameters for each system that are independent of the models that we test are listed in Table 10. Stellar parameters for HAT-P-44, and parameters of the transiting planet HAT-P-44b, that depend on the class of model tested are listed in Table 11, while parameters for the candidate outer component HAT-P-44c are listed in Table 12. In both cases we only show results for the fiducial model of a single transiting planet and for those models that have $|\ln K - \ln K_{11}| < 5$, where K_{11} is the Bayes factor for model 11, which has the highest evidence. Stellar parameters for HAT-P-45 and HAT-P-46, and parameters for the transiting planets HAT-P-45b and HAT-P-46b that depend on the class of model tested are listed in Table 13, while parameters for the candidate outer component HAT-P-45c and HAT-P-46c are listed in Table 14. For both systems we only show parameters for models 1 and 2, which have the highest Bayesian evidences.

For HAT-P-44 we find that the preferred model, based on the estimated Bayes Factor, consists of two planets, the outer one on an eccentric orbit. This model, labeled number 11 in Tables 9, 11, and 12, includes: the transiting planet HAT-P-44b with a period of $P = 4.301219 \pm 0.000019$ days, a mass of $M_p = 0.352 \pm 0.029$ M_{J}, and an eccentricity of $e = 0.044 \pm 0.052$; an outer planet HAT-P-44c with a period of $P = 872.2 \pm 1.7$ days, a minimum mass of $M_p \sin i = 4.0^{+1.4}_{-0.8}$ M_{J}, and an eccentricity of $e = 0.494 \pm 0.081$. We find that we are not able to definitively choose this model over alternative models, labeled numbers 2, 3, and 4, which are similar in form to the preferred model, but with different periods for the outer planet ($P = 220$ days, or $P = 438$ days). Note that due to the sharpness of the peaks in the likelihood as a function of the period of the outer planet, an MCMC simulation takes an excessively long time to transition between the different periods. For this reason we treat these as independent models. We adopt the model with the long period and high eccentricity for the outer component because it has the highest Bayes factor. This model is favored over the fiducial model of a single planet transiting the

Table 9
Bayes Factor and BIC Differences for Models Tested

Model[a] Number	P_c[b]	e_c[c]	P_d	e_d	Trend Order	N_p[d]	ln(K)[e]	Fixed Jitter ln(K)[f]	ΔBIC[g]
HAT-P-44									
2	220	...	...	...	...	7	10.4	90.7	46.9
3	438	...	...	...	...	7	10.2	89.7	45.2
4	221	✓	...	...	...	9	8.9	90.6	46.3
5	219	...	17	...	...	10	3.1	86.0	57.7
6	219	✓	17	...	...	12	−22.5	82.9	54.9
7	216	✓	18	✓	...	14	2.5	82.0	59.2
8	...	...	...	...	1	6	−2.8	9.5	0.9
9	...	...	...	...	2	7	3.2	76.1	32.3
10	1981	...	...	...	...	7	5.4	94.7	32.2
11	872	✓	...	...	...	9	12.4	95.2	54.5
HAT-P-45									
2	15.3	...	...	...	...	7	−3.0	−10.1	29.2
3	...	...	...	...	2	6	−10.7	−10.6	−1.0
HAT-P-46									
2	78	...	...	...	...	7	2.8	55.3	38.8
3	78	✓	...	...	...	9	−4.2	51.3	35.9
4	78	...	8.1	...	...	10	−7.5	48.1	46.2
5	...	...	...	...	1	6	−4.7	−12.7	−2.0
6	...	...	...	...	2	7	−12.8	−15.2	−3.4

Notes.

[a] The number associated with this model in Tables 11–14. Model 1 for each system is the fiducial model of a single planet on an eccentric orbit. By definition this model has $\ln(K) = 0$ and $\Delta\mathrm{BIC} = 0$.

[b] The orbital period used for component c or d in days. Models for which the period of a component is listed as "..." did not include that planet. We list here the median value from the posterior distribution for this parameter. For HAT-P-44 model 10, this value is substantially different from the value of $P = 872$ d used to initialize the fit.

[c] Flag indicating whether or not the component is allowed to be eccentric (indicated by a ✓), or if the eccentricity was fixed to 0 (indicated by "...").

[d] Number of varied parameters constrained by the RV observations, including four parameters for the inner transiting planet and one parameter for the jitter. Although the two parameters used to describe the ephemeris of the inner planet are varied in the joint fit of the RV and photometric data, they are almost entirely determined by the photometric data alone, so we do not include them in this accounting.

[e] The natural logarithm of the Bayes Factor between the given model, and a fiducial model of a single planet on an eccentric orbit. Models with higher values of $\ln K$ are preferred. In this case the RV jitter is allowed to vary in the fit, subject to a prior constraint from the empirical jitter distribution found by Wright (2005).

[f] The natural logarithm of the Bayes Factor between the given model, and a fiducial model of a single planet on an eccentric orbit. In this case the RV jitter is fixed to a typical value for each star (these were determined such that χ^2 per degree of freedom was unity for one of the models; we adopted 9.1 m s^{-1} for HAT-P-44, 12.7 m s^{-1} for HAT-P-45, and 2.7 m s^{-1} for HAT-P-46). We provide these to show how the model selection depends on the method for treating the RV jitter.

[g] $\Delta\mathrm{BIC} = \mathrm{BIC}_{\mathrm{fiducial}} - \mathrm{BIC}_{\mathrm{model}}$, i.e., the difference between the BIC for the fiducial model and for the given model. Models with higher values of ΔBIC are preferred.

Table 10
Model-independent Stellar and Light Curve Parameters for HAT-P-44–HAT-P-46

Parameter	HAT-P-44b Value	HAT-P-45b Value	HAT-P-46b Value	Source[a]
Stellar astrometric properties				
GSC ID	GSC 3465-00123	GSC 5102-00262	GSC 5100-00045	
2MASS ID	2MASS 14123457+4700528	2MASS 18172957-0322517	2MASS 18014660-0258154	
R.A. (J2000)	$14^h12^m34^s.56$	$18^h17^m29^s.40$	$18^h01^m46^s.56$	
Decl. (J2000)	$+47°00'52''.9$	$-03°22'51''.7$	$-02°58'15''.4$	
$\mu_{\rm R.A.}$ (mas yr^{-1})	-29.0 ± 12.6	9.2 ± 4.1	-7.5 ± 4.3	
$\mu_{\rm Decl.}$ (mas yr^{-1})	12.3 ± 11.4	-3.1 ± 8.2	2.0 ± 7.9	
Stellar spectroscopic properties				
$T_{\rm eff\star}$ (K)	5295 ± 100	6330 ± 100	6120 ± 100	SME[b]
[Fe/H]	0.33 ± 0.10	0.07 ± 0.10	0.30 ± 0.10	SME
$v \sin i$ (km s^{-1})	0.2 ± 0.5	9.3 ± 0.5	4.9 ± 0.5	SME
v_{mac} (km s^{-1})	3.28	4.88	4.55	SME
v_{mic} (km s^{-1})	0.85	0.85	0.85	SME
$\gamma_{\rm RV}$ (km s^{-1})	-33.45 ± 0.05	23.903 ± 0.1	-20.911 ± 0.1	TRES
$\log R'_{\rm HK}$	$-5.247 \pm 0.058 \pm 0.10$	$-5.394 \pm 0.072 \pm 0.25$	$-5.257 \pm 0.036 \pm 0.21$	Keck/HIRES[c]
Stellar photometric properties				
V (mag)	13.21 ± 0.12	12.79 ± 0.18	11.94 ± 0.12	TASS
$V - I_C$ (mag)	0.90 ± 0.24	1.11 ± 0.19	0.87 ± 0.14	TASS
J (mag)	11.729 ± 0.021	10.730 ± 0.027	10.330 ± 0.024	2MASS
H (mag)	11.360 ± 0.019	10.350 ± 0.026	9.972 ± 0.022	2MASS
K_s (mag)	11.275 ± 0.018	10.201 ± 0.023	9.924 ± 0.023	2MASS
Transiting planet light curve parameters				
P (days)	4.301219 ± 0.000019	3.128992 ± 0.000021	4.463129 ± 0.000048	
T_c (BJD)[d]	$2455696.93695 \pm 0.00024$	$2455729.98612 \pm 0.00041$	$2455701.33646 \pm 0.00047$	
T_{14} (days)[d]	0.1302 ± 0.0008	0.1436 ± 0.0013	0.1291 ± 0.0018	
$T_{12} = T_{34}$ (days)[d]	0.0158 ± 0.0006	0.0154 ± 0.0011	0.0174 ± 0.0017	
$\zeta/R_\star$	17.49 ± 0.07	15.60 ± 0.08	17.83 ± 0.13	
$R_p/R_\star$	0.1343 ± 0.0010	0.1110 ± 0.0021	0.0942 ± 0.0017	
b^2	$0.030^{+0.037}_{-0.018}$	$0.079^{+0.058}_{-0.043}$	$0.392^{+0.047}_{-0.059}$	
$b \equiv a \cos i/R_\star$	$0.172^{+0.079}_{-0.074}$	$0.281^{+0.085}_{-0.106}$	$0.626^{+0.036}_{-0.051}$	
Assumed limb-darkening coefficients[e]				
c_1, i (linear term)	0.3648	0.1935	0.2222	Claret (2004)
c_2, i (quadratic term)	0.2817	0.3680	0.3651	Claret (2004)

Notes.
[a] We list the source only for the stellar properties. The listed transiting planet light curve parameters are determined from our joint fit of the RV and light curve data, but are primarily constrained by the light curves.
[b] SME = "Spectroscopy Made Easy" package for the analysis of high-resolution spectra (Valenti & Piskunov 1996). These parameters rely primarily on SME, but have a small dependence also on the iterative analysis incorporating the isochrone search and global modeling of the data, as described in the text.
[c] Median values of $\log R'_{\rm HK}$ (Noyes et al. 1984) are computed from the Keck/HIRES spectra following the procedure of Isaacson & Fischer (2010). Uncertainties are the standard error on the median given the scatter in the individual measurements, followed by our estimate of the systematic uncertainty assuming an uncertainty of 11% in the calibration of S (Isaacson & Fischer 2010). Note that this index has not been calibrated for stars with $T_{\rm eff\star} \gtrsim 6200$ K so the results for HAT-P-45 and HAT-P-46, which are above and just below this threshold, should be treated with caution.
[d] T_c: reference epoch of mid transit that minimizes the correlation with the orbital period. T_{14}: total transit duration, time between first to last contact; $T_{12} = T_{34}$: ingress/egress time, time between first and second, or third and fourth contact. Barycentric Julian dates (BJD) throughout the paper are calculated from Coordinated Universal Time (UTC).
[e] Values for a quadratic law.

host star by a factor of $\sim 2 \times 10^5$, indicating that the data strongly favor the two-planet model over the single-planet model. The preferred model has an associated jitter of 10.7 ± 2.0 m s^{-1} and a χ^2 per degree of freedom, including this jitter, of 1.67. Based on Equation (1), one expects only 1.2% of stars like HAT-P-44 to have jitter values $\geqslant 10.7$ m s^{-1} thus the excess scatter in the RV residuals from the best-fit two-planet model suggests that perhaps more than two planets are present in this system, though we cannot conclusively detect any additional planets from the data currently available.

For HAT-P-45 the fiducial model of a single planet on an eccentric orbit is preferred over the other models that we tested. This model, labeled number 1 under the HAT-P-45 headings in Tables 9, 13, and 14, includes only the transiting planet HAT-P-45b with a period of $P = 3.128992 \pm 0.000021$ days, a mass of $M_p = 0.892^{+0.137}_{-0.099}\, M_{\rm J}$, and an eccentricity of $e = 0.049 \pm 0.063$. The preferred model has a jitter of 22.5 ± 6.3 m s^{-1} and χ^2 per degree of freedom of 2.1. Only $\sim$0.8% of stars like HAT-P-45 are expected to have a jitter this high. Moreover, the RV residuals from the preferred best-fit model appear to show a variation that is correlated in time (see the third panel down in Figure 3). Both these factors may suggest that a second planet is in the HAT-P-45 system. Nonetheless the data do not at present support such a complicated model. The single-planet model has a Bayes

Table 11
Model-dependent System Parameters for HAT-P-44

Parameter	Model 1 Value	Model 2 Value	Model 3 Value	Model 4 Value	Adopted Model 11 Value
Transiting planet (HAT-P-44b) light curve parameters					
$a/R_\star$	9.34 ± 1.70	$11.11^{+0.70}_{-1.03}$	10.13 ± 1.08	$11.37^{+0.54}_{-0.97}$	$11.49^{+0.46}_{-0.85}$
i (deg)	$88.7^{+0.6}_{-1.6}$	89.0 ± 0.5	$88.8^{+0.5}_{-0.8}$	89.1 ± 0.5	89.1 ± 0.4
Transiting planet (HAT-P-44b) RV parameters					
K (m s^{-1})	47.1 ± 10.7	51.5 ± 3.9	52.5 ± 4.7	48.1 ± 4.1	45.9 ± 3.6
$\sqrt{e}\cos\omega$	$-0.206^{+0.257}_{-0.189}$	-0.006 ± 0.121	-0.113 ± 0.113	-0.046 ± 0.125	-0.023 ± 0.121
$\sqrt{e}\sin\omega$	$0.421^{+0.172}_{-0.312}$	$0.219^{+0.151}_{-0.236}$	$0.364^{+0.122}_{-0.231}$	0.147 ± 0.185	0.114 ± 0.175
$e\cos\omega$	-0.099 ± 0.129	-0.001 ± 0.037	-0.041 ± 0.047	$-0.008^{+0.030}_{-0.042}$	-0.003 ± 0.032
$e\sin\omega$	0.214 ± 0.170	$0.055^{+0.098}_{-0.059}$	0.144 ± 0.103	$0.029^{+0.092}_{-0.042}$	$0.019^{+0.080}_{-0.036}$
e	0.272 ± 0.155	0.072 ± 0.071	0.158 ± 0.098	0.054 ± 0.062	0.044 ± 0.052
ω (deg)	117 ± 50	98 ± 84	108 ± 44	114 ± 82	113 ± 90
RV jitter (m s^{-1})	31.0 ± 4.2	12.7 ± 2.5	13.4 ± 2.3	11.5 ± 2.1	10.7 ± 2.0
Derived transiting planet (HAT-P-44b) parameters					
M_p (M_J)	0.347 ± 0.077	0.392 ± 0.031	0.394 ± 0.036	0.368 ± 0.033	0.352 ± 0.029
R_p (R_J)	$1.523^{+0.442}_{-0.226}$	$1.280^{+0.145}_{-0.074}$	$1.403^{+0.190}_{-0.130}$	$1.256^{+0.126}_{-0.059}$	$1.242^{+0.106}_{-0.051}$
$C(M_p, R_p)$[a]	0.18	0.10	0.11	0.16	0.06
ρ_p (g cm^{-3})	$0.12^{+0.09}_{-0.05}$	0.23 ± 0.05	$0.18^{+0.07}_{-0.05}$	0.23 ± 0.05	0.23 ± 0.04
$\log g_p$ (cgs)	2.55 ± 0.19	$2.77^{+0.06}_{-0.09}$	2.69 ± 0.10	$2.75^{+0.06}_{-0.08}$	$2.75^{+0.05}_{-0.07}$
a (AU)	$0.0509^{+0.0014}_{-0.0008}$	0.0507 ± 0.0007	0.0507 ± 0.0008	0.0507 ± 0.0007	0.0507 ± 0.0007
$T_{\rm eq}$ (K)	1238^{+173}_{-107}	1126^{+67}_{-42}	1181^{+84}_{-64}	1114^{+59}_{-36}	1108^{+51}_{-32}
Θ[b]	0.024 ± 0.007	0.033 ± 0.003	0.030 ± 0.004	0.031 ± 0.003	0.030 ± 0.003
$\langle F \rangle$ [c]	$5.30^{+4.25}_{-1.54}$	$3.63^{+1.02}_{-0.50}$	$4.40^{+1.49}_{-0.85}$	$3.48^{+0.86}_{-0.42}$	$3.40^{+0.72}_{-0.37}$
Derived stellar properties					
$M_\star$ ($M_\odot$)	$0.953^{+0.083}_{-0.045}$	0.939 ± 0.041	0.938 ± 0.042	0.941 ± 0.041	0.942 ± 0.041
$R_\star$ ($R_\odot$)	$1.165^{+0.334}_{-0.173}$	$0.979^{+0.110}_{-0.055}$	$1.072^{+0.144}_{-0.099}$	$0.960^{+0.096}_{-0.043}$	$0.949^{+0.080}_{-0.037}$
$\log g_\star$ (cgs)	4.28 ± 0.16	4.43 ± 0.07	4.35 ± 0.09	4.45 ± 0.06	4.46 ± 0.06
$L_\star$ ($L_\odot$)	$0.96^{+0.71}_{-0.27}$	$0.68^{+0.19}_{-0.10}$	$0.81^{+0.27}_{-0.16}$	$0.66^{+0.16}_{-0.09}$	$0.64^{+0.14}_{-0.08}$
M_V (mag)	4.97 ± 0.46	5.34 ± 0.23	5.15 ± 0.28	5.38 ± 0.21	5.41 ± 0.19
M_K (mag,ESO)	3.06 ± 0.44	3.44 ± 0.19	3.24 ± 0.24	3.48 ± 0.16	3.50 ± 0.14
Age (Gyr)	$11.5^{+3.3}_{-4.4}$	8.9 ± 3.9	11.5 ± 3.8	8.1 ± 3.8	7.5 ± 3.6
A_V (mag)	0.000 ± 0.083	0.000 ± 0.081	0.000 ± 0.083	0.000 ± 0.080	0.000 ± 0.080
Distance (pc)	445^{+127}_{-66}	374^{+42}_{-23}	409^{+55}_{-39}	367^{+37}_{-19}	363^{+31}_{-17}

Notes.
[a] Correlation coefficient between the planetary mass M_p and radius R_p.
[b] The Safronov number is given by $\Theta = 1/2(V_{\rm esc}/V_{\rm orb})^2 = (a/R_p)(M_p/M_\star)$ (see Hansen & Barman 2007).
[c] Incoming flux per unit surface area, averaged over the orbit, measured in units of 10^8 erg s^{-1} cm^{-2}.

Table 12
Model-dependent Parameters for Outer Planet in HAT-P-44

Parameter	Model 1 Value	Model 2 Value	Model 3 Value	Model 4 Value	Adopted Model 11 Value
RV and derived parameters for candidate planet HAT-P-44c					
P_c (days)	...	219.9 ± 4.5	437.5 ± 17.7	221.4 ± 4.4	872.2 ± 1.7
$T_{c,c}$ (BJD)[a]	...	2455686.2 ± 4.1	2455727.0 ± 4.5	2455713.4 ± 4.3	2455711.2 ± 13.4
$T_{14,c}$ (days)[a]	...	0.505 ± 0.039	0.691 ± 0.067	0.652 ± 0.091	0.503 ± 0.047
K_c (m s^{-1})	...	56 ± 6	104 ± 12	93 ± 4	99 ± 33
$\sqrt{e}\cos\omega_c$	...	0	0	-0.373 ± 0.105	-0.453 ± 0.152
$\sqrt{e}\sin\omega_c$	...	0	0	-0.474 ± 0.113	0.510 ± 0.103
$e\cos\omega_c$	...	0	0	-0.226 ± 0.071	-0.313 ± 0.124
$e\sin\omega_c$	...	0	0	$-0.286^{+0.079}_{-0.103}$	0.349 ± 0.078
e_c	...	0	0	0.379 ± 0.075	0.494 ± 0.081
ω_c (deg)	...	0	0	232.1 ± 13.3	131.3 ± 14.4
$M_p \sin i_c$ (M_J)	...	1.6 ± 0.2	3.7 ± 0.5	2.5 ± 0.1	$4.0^{+1.4}_{-0.8}$
a_c (AU)	...	0.699 ± 0.014	$1.104^{+0.039}_{-0.027}$	0.702 ± 0.014	1.752 ± 0.025

Note. [a] T_c: reference epoch of mid transit that minimizes the correlation with the orbital period. T_{14}: total transit duration, time between first to last contact; Barycentric Julian dates (BJD) throughout the paper are calculated from Coordinated Universal Time (UTC).

Table 13
Model-dependent System Parameters for HAT-P-45 and HAT-P-46

Parameter	HAT-P-45		HAT-P-46	
	Adopted Model 1 Value	Model 2 Value	Model 1 Value	Adopted Model 2 Value
Transiting planet (HAT-P-45b and HAT-P-46b) light curve parameters				
$a/R_\star$	$7.36^{+0.39}_{-0.62}$	7.56 ± 0.31	$8.84^{+1.04}_{-1.76}$	$8.86^{+0.89}_{-1.24}$
i (deg)	87.8 ± 0.9	87.9 ± 0.8	$85.4^{+1.0}_{-4.1}$	$85.5^{+0.8}_{-2.3}$
Transiting planet (HAT-P-45b and HAT-P-46b) RV parameters				
K (m s^{-1})	106.6 ± 13.6	106.9 ± 4.5	40.9 ± 19.7	52.2 ± 6.8
$\sqrt{e}\cos\omega$	-0.009 ± 0.160	-0.031 ± 0.086	$0.180^{+0.239}_{-0.317}$	$0.143^{+0.098}_{-0.134}$
$\sqrt{e}\sin\omega$	0.045 ± 0.192	-0.084 ± 0.131	0.242 ± 0.269	$0.305^{+0.170}_{-0.258}$
$e\cos\omega$	$-0.001^{+0.061}_{-0.045}$	-0.004 ± 0.017	$0.064^{+0.183}_{-0.140}$	$0.047^{+0.066}_{-0.042}$
$e\sin\omega$	$0.006^{+0.089}_{-0.045}$	$-0.010^{+0.024}_{-0.039}$	$0.091^{+0.217}_{-0.108}$	$0.105^{+0.149}_{-0.089}$
e	0.049 ± 0.063	0.025 ± 0.026	0.195 ± 0.167	0.123 ± 0.120
ω (deg)	146 ± 98	239 ± 87	82 ± 113	70 ± 87
RV jitter (m s^{-1})	22.5 ± 6.3	4.7 ± 3.5	28.4 ± 6.7	6.6 ± 3.0
Derived transiting planet (HAT-P-45b and HAT-P-46b) parameters				
M_p (M_J)	$0.892^{+0.137}_{-0.099}$	0.890 ± 0.046	$0.383^{+0.218}_{-0.127}$	$0.493^{+0.082}_{-0.052}$
R_p (R_J)	$1.426^{+0.175}_{-0.087}$	1.382 ± 0.076	$1.286^{+0.426}_{-0.150}$	$1.284^{+0.271}_{-0.133}$
$C(M_p, R_p)$[a]	0.45	0.40	0.43	0.72
ρ_p (g cm^{-3})	0.38 ± 0.09	0.42 ± 0.06	$0.20^{+0.14}_{-0.09}$	0.28 ± 0.10
$\log g_p$ (cgs)	3.03 ± 0.07	3.06 ± 0.04	$2.72^{+0.16}_{-0.28}$	2.86 ± 0.10
a (AU)	0.0452 ± 0.0007	0.0451 ± 0.0006	$0.0577^{+0.0020}_{-0.0010}$	$0.0577^{+0.0014}_{-0.0009}$
$T_{\rm eq}$ (K)	1652^{+90}_{-52}	1627 ± 44	1465^{+220}_{-89}	1458^{+140}_{-75}
Θ[b]	0.044 ± 0.006	0.046 ± 0.003	0.025 ± 0.009	0.034 ± 0.004
$\langle F \rangle$ [c]	$1.68^{+0.44}_{-0.20}$	1.58 ± 0.17	$1.04^{+0.89}_{-0.22}$	$1.02^{+0.50}_{-0.19}$
Derived stellar properties				
$M_\star$ ($M_\odot$)	1.259 ± 0.058	1.246 ± 0.050	$1.289^{+0.144}_{-0.068}$	$1.284^{+0.095}_{-0.060}$
$R_\star$ ($R_\odot$)	$1.319^{+0.155}_{-0.072}$	1.281 ± 0.060	$1.398^{+0.465}_{-0.156}$	$1.396^{+0.293}_{-0.136}$
$\log g_\star$ (cgs)	4.30 ± 0.06	4.32 ± 0.03	4.25 ± 0.15	4.25 ± 0.11
$L_\star$ ($L_\odot$)	$2.51^{+0.71}_{-0.33}$	2.35 ± 0.30	$2.48^{+2.08}_{-0.57}$	$2.46^{+1.25}_{-0.49}$
M_V (mag)	3.75 ± 0.21	3.83 ± 0.15	3.78 ± 0.47	3.79 ± 0.34
M_K (mag,ESO)	2.58 ± 0.18	2.65 ± 0.11	2.47 ± 0.46	2.48 ± 0.32
Age (Gyr)	2.0 ± 0.8	1.7 ± 0.8	$2.4^{+0.7}_{-1.0}$	$2.5^{+0.7}_{-1.0}$
A_V (mag)	1.900 ± 0.169	1.895 ± 0.167	0.831 ± 0.145	0.832 ± 0.145
Distance (pc)	305^{+35}_{-17}	296 ± 14	296^{+98}_{-33}	296^{+61}_{-29}

Notes.
[a] Correlation coefficient between the planetary mass M_p and radius R_p.
[b] The Safronov number is given by $\Theta = 1/2(V_{\rm esc}/V_{\rm orb})^2 = (a/R_p)(M_p/M_\star)$ (see Hansen & Barman 2007).
[c] Incoming flux per unit surface area, averaged over the orbit, measured in units of 10^8 erg s^{-1} cm^{-2}.

factor of ∼20 relative to the two-planet model, indicating a slight preference for the single-planet model. We also note that the BSs and RV residuals from the single-planet model may be correlated. A Spearman rank-order correlation test (e.g., Press et al. 1992) yields a correlation coefficient of $r_s = 0.54$ which indicates a weak correlation with a 10% false alarm probability. A correlation between these quantities suggests that at least some of the excess RV scatter in this system may due to stellar activity.

For HAT-P-46 the preferred model consists of a transiting planet together with an outer companion on a circular orbit. This model, labeled number 2 under the HAT-P-46 headings in Tables 9, 13, and 14, includes: the transiting planet HAT-P-46b with a period of $P = 4.463129 \pm 0.000048$ days, a mass of $M_p = 0.493^{+0.082}_{-0.052}$ M_J, and an eccentricity of $e = 0.123 \pm 0.120$; and an outer planet HAT-P-46c with a period of $P = 77.7 \pm 0.6$ days, and a minimum mass of $M_p \sin i = 2.0 \pm 0.3$ M_J. Although the two-planet model is preferred, it has a Bayes factor of only $K \sim 16$ relative to the fiducial single-planet model, indicating that the preference is not very strong. The preferred model has a jitter of 6.6 ± 3.0 m s^{-1} and χ^2 per degree of freedom of 1.6. The resulting jitter is typical for a star like HAT-P-46 (∼25% of such stars have a jitter higher than 6.6 ± 3.0 m s^{-1}), so there is no compelling reason at present to suspect that there may be more planets in this system beyond HAT-P-46c.

For both HAT-P-44 and HAT-P-46 allowing the jitter to vary in the fit substantially reduces the significance of the multi-planet solutions relative to the single planet solution. If we had not allowed the jitter to vary, we would have concluded that the two-planet model is $\sim 10^{39}$ times more likely than the one-planet model for HAT-P-44, and $\sim 10^{24}$ times more likely for HAT-P-46. For HAT-P-45, it is interesting to note that allowing the jitter to vary actually increases the significance of the

Table 14
Model-dependent Parameters for Outer Planets in HAT-P-45 and HAT-P-46

Parameter	HAT-P-45		HAT-P-46	
	Adopted Model 1 Value	Model 2 Value	Model 1 Value	Adopted Model 2 Value
RV and derived parameters for candidate planets HAT-P-45c, HAT-P-46c				
P_c (days)	...	15.3 ± 0.1	...	77.7 ± 0.6
$T_{c,c}$ (BJD)[a]	...	2455700.0 ± 0.3	...	2455695.6 ± 2.0
$T_{14,c}$ (days)[a]	...	0.242 ± 0.009	...	0.446 ± 0.058
K_c ($m\,s^{-1}$)	...	36 ± 5	...	81 ± 9
$\sqrt{e}\cos\omega_c$	...	0	...	0
$\sqrt{e}\sin\omega_c$	...	0	...	0
$e\cos\omega_c$	...	0	...	0
$e\sin\omega_c$	...	0	...	0
e_c	...	0	...	0
ω_c (deg)	...	0	...	0
$M_p \sin i_c$ (M_J)	...	0.5 ± 0.1	...	2.0 ± 0.3
a_c (AU)	...	0.130 ± 0.002	...	$0.387^{+0.010}_{-0.007}$

Notes. [a] T_c: reference epoch of mid transit that minimizes the correlation with the orbital period. T_{14}: total transit duration, time between first to last contact; Barycentric Julian dates (BJD) throughout the paper are calculated from Coordinated Universal Time (UTC).

two-planet model, perhaps due to the relatively high jitter value that must be adopted to achieve $\chi^2/\mathrm{dof} = 1$.

3.5.1. Orbital Stability

To check the orbital stability of the multi-planet solutions that we have found, we integrated each orbital configuration forward in time for a duration of 1 Myr using the Mercury symplectic integrator (Chambers 1999). We find that the adopted solutions for HAT-P-44 and HAT-P-46 are stable over at least this time period, and should be stable for much longer given the large, and non-resonant, period ratio between the components in each case. For HAT-P-44 the three-planet models that we tested quickly evolved in less than 10^4 years to a different orbital configuration. In particular, when we start HAT-P-44b on a 4.3012 day period, HAT-P-44c on a 215.7 ± 3.9 day period, and HAT-P-44d on a 17.6 ± 0.2 day period, HAT-P-44d migrates to a 15.1 day period orbit, while HAT-P-44b migrates to a 4.6928 day period. While this final configuration appears to be stable for at least 4×10^5 yr, it is inconsistent with the RV and photometric data. We did not carry out a full exploration of the parameter space allowed by our uncertainties, but the fact that the best-fit three-planet model for HAT-P-44 shows rapid planetary migration indicates that this model may very well be unstable. If additional RV observations support a three-planet solution for HAT-P-44, it will also be important to test the stability of this solution.

4. DISCUSSION

We have presented the discovery of three new transiting planet systems. The inner transiting planets have masses, radii, and orbital periods typical of other hot Jupiters. The planets are located on well occupied areas of both the mass–radius and the equilibrium temperature–radius diagrams. Nonetheless, as objects with well measured masses and radii, these planets will be important contributors to statistical studies of exoplanetary systems.

A notable feature of all three systems is the systematic variation seen in each of their residual RV curves. We allow in our modeling for the possibility that this excess scatter can be attributed to jitter using the empirical jitter distribution from Keck/HIRES as a prior constraint. To our knowledge this is the first time an empirical constraint on the jitter has been used in modeling the RV data for a transiting exoplanet system. Using the empirical jitter distribution significantly affects the conclusions: if we had fixed the jitter to a typical value, or a value where $\chi^2/\mathrm{dof} = 1$ for the best-fit model, we would have claimed with much greater confidence the existence of multiple planets in each system. Accounting for the uncertainty in the jitter, which must be inferred from the observations, leads to a lower confidence that we believe is more realistic.

We find that for two of the targets, HAT-P-44 and HAT-P-46, a two-planet model best explains the observations. HAT-P-44 appears to have, in addition to the $P = 4.3012$ day transiting planet, a long period planet on a $P = 872$ day, $P = 220$ day, or $P = 438$ day orbit, where the ambiguity is due to aliasing. HAT-P-46 appears to have a $P = 4.4631$ day transiting planet, and a long period planet on a $P = 78$ day orbit, though we caution that the preference for this model over a single-planet model is not very strong for this system. Due to the limited number of RV observations, we are unable to confirm that the variation in the HAT-P-45 residual RV curve is due to a second planet, rather than being the result of anomalously high jitter for this star. Nonetheless, the high scatter, and apparent temporal correlation in that scatter, are both suggestive of a second planet, though could also be due to stellar activity.

As noted in the introduction, outer planetary companions have been confirmed for only five hot Jupiter systems (υ And; HD 217107; HD 187123; HIP 14810; and HAT-P-13). Only one of these, HAT-P-13, is a transiting planet system. In several other cases long-term trends have been detected, but so far the periods have not been constrained. For both HAT-P-44 and HAT-P-46 the periods of the outer planets in our adopted models are significantly longer than the transiting planet periods. This is in line with the five previously known multi-planet hot-Jupiter-bearing systems, where the shortest period outer component is HIP 14810c with a period of 147.8 days, and is unlike other multi-planet systems where densely packed systems with components having similar periods appear to be common (e.g., Lissauer et al. 2011; Fabrycky et al. 2012).

Another interesting aspect of the three systems presented here is that they all have super-solar metallicities ([Fe/H] = 0.33 ± 0.10, 0.07 ± 0.10, and 0.30 ± 0.10 for HAT-P-44, HAT-P-45, and HAT-P-46, respectively), as do the five confirmed multi-planet hot Jupiter systems ([Fe/H] = 0.153 ± 0.03, 0.389 ± 0.03, 0.121 ± 0.03, 0.230 ± 0.03, and 0.410 ± 0.08 for υ And, HD 217107, HD 187123, HIP 14810, and HAT-P-13, respectively). That giant planets are more common around metal-rich stars is well known (Fischer & Valenti 2005); moreover, evidence suggests that the relation between metallicity and occurrence is even stronger for multi-planet systems than it is for single planet systems (e.g., Wright et al. 2009). Recently Dawson & Murray-Clay (2013) suggested that giant planets orbiting metal-rich stars are more likely to show signatures of planet–planet interactions. Of the 166 hot-Jupiter-hosting stars in the exoplanets orbit database with measured metallicities, 109 have [Fe/H] > 0 and 57 have [Fe/H] < 0. While there is a 12% probability of finding 5 systems with [Fe/H] > 0 if $109/(57+109) = 66\%$ of systems have such a metallicity, if we include HAT-P-44 and HAT-P-46 then the probability decreases to 5%. A Kolmogorov–Smirnov (K-S) test yields a 0.6% chance that the sample of seven multi-planet hot Jupiter systems (including HAT-P-44 and HAT-P-46) have metallicities drawn from the same distribution as all hot Jupiter-hosting systems. However, if we compare the multi-planet hot Jupiter-hosting systems to the 48 multi-planet systems with metallicities in the database that have at least one component with $M_P \sin i > 0.1\ M_J$, the K-S test yields a 23% chance that the metallicities are drawn from the same distribution. We conclude that multi-planet systems with Hot Jupiters may be more common around metal rich stars than single Hot Jupiters, to a similar extent that multi-planet systems with giant planets are in general more likely to be found around metal rich stars. A more definitive conclusion requires a careful consideration of selection effects, and a uniform determination of metallicities.

Multi-planet systems with transiting components are potentially useful for a number of applications. For example, RV observations during transit can be used to determine the projected obliquity of the transiting planet via the Rossiter–McLaughlin effect (e.g., Queloz et al. 2000). Measuring this angle for several systems would test whether the orientations of hot Jupiters in multi-planet systems are significantly different from isolated hot Jupiters, thereby testing if these two classes of systems have experienced different formation and/or evolution processes. Another example is the tidal Love number, which carries information about the interiors of planets, and can potentially be determined for transiting planets in multi-planet systems (Batygin et al. 2009; Mardling 2010; Kramm et al. 2012).

While we have explored numerous classes of models for each system, we have not exhausted all possibilities, and it may be that the any one of these systems has a planetary architecture that is substantially different from what we have considered in this paper. Further long-term RV monitoring of these objects is needed to confirm the outer planets in these systems and characterize their properties.

HATNet operations have been funded in part by NASA grants NNG04GN74G, NNX08AF23G, and NNX13AJ15G. J.D.H., G.Á.B., and W.B. received partial support from NSF grant AST-1108686. G.Á.B., Z.C., and K.P. acknowledge partial support from NASA grant NNX09AB29G. G.T. acknowledges partial support from NASA grant NNX09AF59G. We acknowledge partial support also from the Kepler Mission under NASA Cooperative Agreement NCC2-1390 (PI: D.W.L.). G.K. thanks the Hungarian Scientific Research Foundation (OTKA) for support through grant K-81373. This research has made use of Keck telescope time granted through NOAO (program A284Hr) and NASA (N154Hr, N108Hr). This paper uses observations obtained with facilities of the Las Cumbres Observatory Global Telescope. Data presented in this paper are based on observations obtained at the HAT station at the Submillimeter Array of SAO, and the HAT station at the Fred Lawrence Whipple Observatory of SAO. We also thank Mount Stromlo Observatory and Siding Spring Observatory for granting us time on the ANU 2.3 m telescope. This research has made use of the Exoplanet Orbit Database and the Exoplanet Data Explorer at http://www.exoplanets.org.

REFERENCES

Adams, E. R., Dupree, A. K., Kulesa, C., & McCarthy, D. 2013, AJ, 146, 9
Albrecht, S., Winn, J. N., Johnson, J. A., et al. 2012, ApJ, 757, 18
Albrecht, S., Winn, J. N., Marcy, G. W., et al. 2013, ApJ, 771, 11
Bakos, G., Noyes, R. W., Kovács, G., et al. 2004, PASP, 116, 266
Bakos, G. Á., Hartman, J. D., Torres, G., et al. 2012, AJ, 144, 19
Bakos, G. Á., Howard, A. W., Noyes, R. W., et al. 2009, ApJ, 707, 446
Bakos, G. Á., Kovács, G., Torres, G., et al. 2007, ApJ, 670, 826
Bakos, G. Á., Torres, G., Pál, A., et al. 2010, ApJ, 710, 1724
Batygin, K., Bodenheimer, P., & Laughlin, G. 2009, ApJL, 704, L49
Bayliss, D., Zhou, G., Penev, K., et al. 2013, AJ, 146, 113
Bonifacio, P., Monai, S., & Beers, T. C. 2000, AJ, 120, 2065
Brown, T. M., Baliber, N., Bianco, F. B., et al. 2013, PASP, 125, 1031
Buchhave, L. A., Bakos, G. Á., Hartman, J. D., et al. 2010, ApJ, 720, 1118
Butler, R. P., Marcy, G. W., Fischer, D. A., et al. 1999, ApJ, 526, 916
Butler, R. P., Marcy, G. W., Vogt, S. S., & Apps, K. 1998, PASP, 110, 1389
Butler, R. P., Marcy, G. W., Williams, E., Hauser, H., & Shirts, P. 1997, ApJL, 474, L115
Butler, R. P., Marcy, G. W., Williams, E., et al. 1996, PASP, 108, 500
Cardelli, J. A., Clayton, G. C., & Mathis, J. S. 1989, ApJ, 345, 245
Carpenter, J. M. 2001, AJ, 121, 2851
Chambers, J. E. 1999, MNRAS, 304, 793
Claret, A. 2004, A&A, 428, 1001
Dawson, R. I., & Murray-Clay, R. A. 2013, ApJL, 767, L24
Droege, T. F., Richmond, M. W., Sallman, M. P., & Creager, R. P. 2006, PASP, 118, 1666
Eastman, J., Gaudi, B. S., & Agol, E. 2013, PASP, 125, 83
Fabrycky, D. C., Lissauer, J. J., Ragozzine, D., et al. 2012, arXiv:1202.6328
Feroz, F., Hobson, M. P., & Bridges, M. 2009, MNRAS, 398, 1601
Fischer, D. A., Marcy, G. W., Butler, R. P., Vogt, S. S., & Apps, K. 1999, PASP, 111, 50
Fischer, D. A., & Valenti, J. 2005, ApJ, 622, 1102
Fulton, B. J., Howard, A. W., Winn, J. N., et al. 2013, ApJ, 772, 80
Fűresz, G. 2008, PhD thesis, Univ. Szeged, Hungary
Gregory, P. C. 2005, ApJ, 631, 1198
Hansen, B. M. S., & Barman, T. 2007, ApJ, 671, 861
Hartman, J. D., Bakos, G. Á., Béky, B., et al. 2012, AJ, 144, 139
Hartman, J. D., Bakos, G. Á., Sato, B., et al. 2011, ApJ, 726, 52
Horne, J. H., & Baliunas, S. L. 1986, ApJ, 302, 757
Howard, A. W., Bakos, G. Á., Hartman, J., et al. 2012, ApJ, 749, 134
Isaacson, H., & Fischer, D. 2010, ApJ, 725, 875
Knutson, H. A., Fulton, B. J., Montet, B. T., et al. 2014, ApJ, 785, 126
Kovács, G., Zucker, S., & Mazeh, T. 2002, A&A, 391, 369
Kramm, U., Nettelmann, N., Fortney, J. J., Neuhäuser, R., & Redmer, R. 2012, A&A, 538, A146
Latham, D. W., Bakos, G. Á., Torres, G., et al. 2009, ApJ, 704, 1107
Latham, D. W., Rowe, J. F., Quinn, S. N., et al. 2011, ApJL, 732, L24
Lissauer, J. J., Ragozzine, D., Fabrycky, D. C., et al. 2011, ApJS, 197, 8
Mandel, K., & Agol, E. 2002, ApJL, 580, L171
Mardling, R. A. 2010, MNRAS, 407, 1048
Noyes, R. W., Hartmann, L. W., Baliunas, S. L., Duncan, D. K., & Vaughan, A. H. 1984, ApJ, 279, 763
Pál, A. 2009, MNRAS, 396, 1737
Pál, A., Bakos, G. Á., Torres, G., et al. 2008, ApJ, 680, 1450
Press, W. H., Teukolsky, S. A., Vetterling, W. T., & Flannery, B. P. 1992, Numerical Recipes in C. The Art of Scientific Computing (New York: Cambridge Univ. Press), 640

Queloz, D., Eggenberger, A., Mayor, M., et al. 2000, A&A, 359, L13
Quinn, S. N., Bakos, G. Á., Hartman, J., et al. 2012, ApJ, 745, 80
Sanchis-Ojeda, R., Fabrycky, D. C., Winn, J. N., et al. 2012, Natur, 487, 449
Schlegel, D. J., Finkbeiner, D. P., & Davis, M. 1998, ApJ, 500, 525
Schwarzenberg-Czerny, A. 1996, ApJL, 460, L107
Skrutskie, M. F., Cutri, R. M., Stiening, R., et al. 2006, AJ, 131, 1163
Sozzetti, A., Torres, G., Charbonneau, D., et al. 2007, ApJ, 664, 1190
ter Braak, C. J. F. 2006, Statistics and Computing, 16, 239
Torres, G., Bakos, G. Á., Kovács, G., et al. 2007, ApJL, 666, L121
Valenti, J. A., & Fischer, D. A. 2005, ApJS, 159, 141
Valenti, J. A., & Piskunov, N. 1996, A&AS, 118, 595
Vogt, S. S., Allen, S. L., Bigelow, B. C., et al. 1994, Proc. SPIE, 2198, 362
Vogt, S. S., Butler, R. P., Marcy, G. W., et al. 2005, ApJ, 632, 638
Weinberg, M. D., Yoon, I., & Katz, N. 2013, arXiv:1301.3156
Wright, J. T. 2005, PASP, 117, 657
Wright, J. T., Fakhouri, O., Marcy, G. W., et al. 2011, PASP, 123, 412
Wright, J. T., Marcy, G. W., Fischer, D. A., et al. 2007, ApJ, 657, 533
Wright, J. T., Upadhyay, S., Marcy, G. W., et al. 2009, ApJ, 693, 1084
Yi, S., Demarque, P., Kim, Y.-C., et al. 2001, ApJS, 136, 417